

# Meshless Methods: An Overview and Recent Developments

T. Belytschko<sup>1</sup>    Y. Krongauz<sup>2</sup>    D. Organ<sup>2</sup>    M. Fleming<sup>2</sup>  
P. Krysl<sup>3</sup>

May 2, 1996

<sup>1</sup>Walter P. Murphy Professor of Civil and Mechanical Engineering, Northwestern University

<sup>2</sup>Research Assistant, Theoretical and Applied Mechanics, Northwestern University

<sup>3</sup>Research Associate, Civil Engineering, Northwestern University

## **Abstract**

Meshless approximations based on moving least squares, kernels, and partitions of unity are examined. It is shown that the three methods are in most cases identical except for the important fact that partitions of unity enable  $p$ -adaptivity to be achieved. Methods for constructing discontinuous approximations and approximations with discontinuous derivatives are also described. Next, several issues in implementation are reviewed: discretization (collocation and Galerkin), quadrature in Galerkin and fast ways of constructing consistent moving least square approximations. The paper concludes with some sample calculations.

# 1 Introduction

The problems of computational mechanics grow ever more challenging. For example, in the simulation of manufacturing processes such as extrusion and molding, it is necessary to deal with extremely large deformations of the mesh while in computations of castings the propagation of interfaces between solids and liquids is crucial. In simulations of failure processes, we need to model the propagation of cracks with arbitrary and complex paths. In the development of advanced materials, methods which can track the growth of phase boundaries and extensive microcracking are required.

These problems are not well suited to conventional computational methods such as finite element, finite volume or finite difference methods. The underlying structure of these methods which originates from their reliance on a mesh is not well suited to the treatment of discontinuities which do not coincide with the original mesh lines. Thus the most viable strategy for dealing with moving discontinuities in methods based on meshes is to remesh in each step of the evolution so that mesh lines remain coincident with the discontinuities throughout the evolution of the problem. This can, of course, introduce numerous difficulties such as the need to project between meshes in successive stages of the problem, which lead to degradation of accuracy and complexity in the computer program, not to mention the burden associated with a large number of remeshings.

The objective of meshless methods is to eliminate at least part of this structure by constructing the approximation entirely in terms of nodes. Although in many meshless methods, recourse must be taken to meshes in at least parts of the method, moving discontinuities can usually be treated without remeshing with minor costs in accuracy degradation. Thus it becomes possible to solve large classes of problems which are very awkward with mesh-based methods.

Although meshless methods originated about twenty years ago, the research effort devoted to them until recently was miniscule. The starting point which seems to have the longest continuous history is the smooth particle hydrodynamics (SPH) method (Lucy, 1977), who used it for modeling astrophysical phenomena without boundaries such as exploding stars and dust clouds. Compared to other methods in these times of prolific academicians, the rate of publications was very modest for many years and is mainly reflected in the papers of Monaghan and coworkers (Monaghan, 1982; Monaghan, 1988). In these papers, the method was explained as a kernel estimate to provide a more rational basis. However, except for some estimates on the accuracy of the kernel estimate, which is not directly relevant to the accuracy of the method in the solution of partial differential equations, there was little in the way of estimation of the accuracy of the method.

Recently, there has been substantial improvement in these methods. Swegle, Hicks, and Attaway (1995) have shown the origin of the so-called tensile instability through a dispersion analysis of the linearized equations and proposed a viscosity

term to stabilize it. Dyka (1994) has proposed stabilization by means of stress particles. Johnson and Beissel (1996) have proposed a method for improving the strain calculation. Liu, Jun, and Zhang (1995) have proposed a correction function for kernels in both the discrete and continuous case.

A parallel path to constructing meshless approximations, which commenced much later, is the use of moving least square approximations. Nayroles et al. (1992) were evidently the first to use moving least square approximations in a Galerkin method called the diffuse element method (DEM). Belytschko, Lu, and Gu (1994) refined and modified the method and called their method EFG, element-free Galerkin. This class of methods is consistent and, in the forms proposed, quite stable, although substantially more expensive than SPH.

Recently a leap has been provided in our understanding of these methods through the work of Duarte and Oden (1996) and Babuška and Melenk (1995). They recognized that the methods based on moving least squares are specific instances of partitions of unity. This enabled them to propose powerful extensions of these approximations, which are discussed later. They and Liu et al. (1996) were also among the first to prove convergence of this class of methods.

Two other paths in the evolution of meshless methods have been the development of generalized finite difference methods which can deal with arbitrary arrangements of nodes and particle-in-cell methods. One of the early contributors to the former was Perrone and Kao (1975), but the more robust of these methods were developed in the 1980's by Liszka and Orkisz (1980). Recently these methods have taken a character which closely resembles moving least squares and partitions of unity, as can be seen from the article by Liszka and coworkers in this volume. Recent progress in particle-in-cell methods is reflected in this volume in the paper by Sulsky and Schreyer.

The first objective of this paper, which we address in Section 2, is to present the salient features of three of the above methods in which we have worked: kernel methods, moving least square methods (MLS), and partition of unity methods. It is shown that the methods share many features of the same framework, and that in most cases, MLS methods are identical to kernel methods: any kernel method in which the parent kernel is identical to the weight function of a MLS approximation and is rendered consistent by the same basis is identical. In other words, a discrete kernel approximation which is consistent must be identical to the related MLS approximation. Furthermore, as pointed out by Duarte and Oden (1996), any MLS approximation may serve as a partition of unity.

In Section 3, we consider the issue of functions with discontinuities and discontinuous derivatives. Approximations of discontinuous fields play an important role in engineering problems. Several methods are reviewed for both cases, but this problem has only been tackled recently, and the proposed methods may not be optimal. Nevertheless, considerable progress has been achieved.

Section 4 deals with the implementation of meshless methods. Collocation meth-

ods and Galerkin methods are reviewed. Some of the major issues in the implementation of MLS and partition of unity methods are discussed, such as the implementation of essential boundary conditions, coupling with finite elements, and speed of computation. Through a synthesis and generalization of MLS and kernel methods, some faster procedures for the calculation of the functions and their derivatives are developed.

Section 5 reviews some work on plates and shells and Section 6 convergence of these meshless methods.

Section 7 provides some examples of meshless calculations obtained with EFG. The first part of these results deal with convergence. The problems include static and dynamic crack propagation in two dimensions and a fully nonlinear problem in three dimensions. We conclude with some reflections on the state of the method.

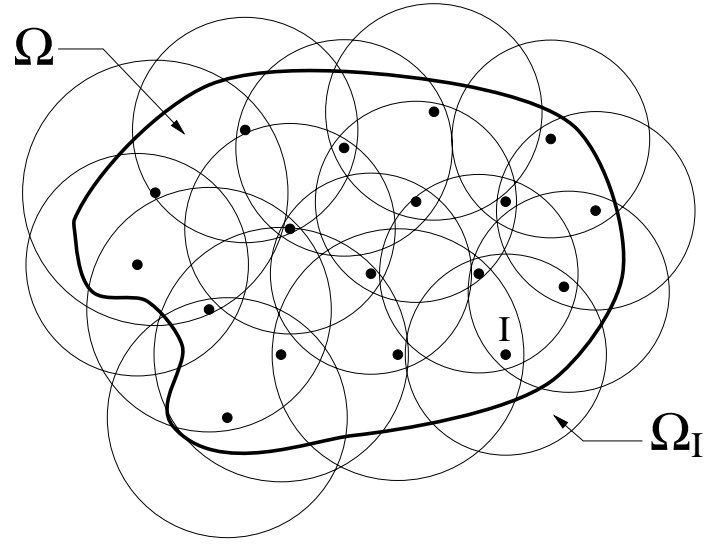
## 2 Meshless Approximation Functions

In this section, various available approximations for meshless methods will be described and examined. For this purpose, we consider the approximation of a single function  $u(\mathbf{x})$  in a domain  $\Omega$ . The domain  $\Omega$  is assumed to be described by the usual methods of computational geometry. Within the domain, a set of nodes  $\mathbf{x}_I$ ,  $I = 1$  to  $n_N$ , is constructed and the parameter associated with the approximation at node  $I$  is denoted by  $u_I$ . We will describe how the meshless approximation is constructed for various methods and examine the consistency of the approximation. We will also compare the different approximations, which will reveal many similarities.

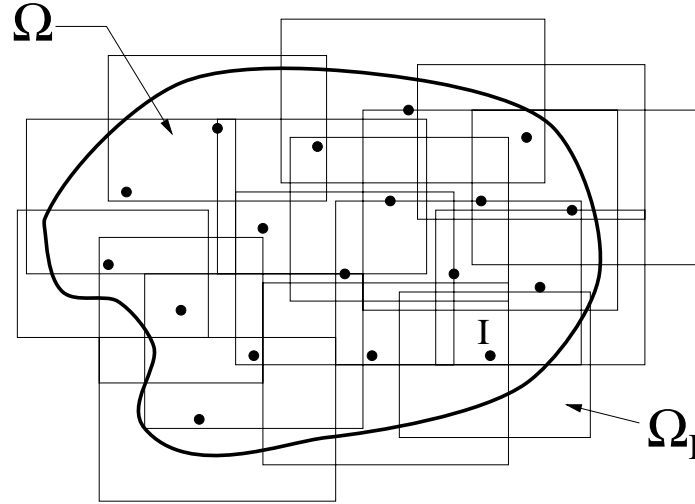
A common feature of all meshless methods is a weight function, or if we use the nomenclature of wavelets, a window function. A weight function is defined to have compact support, i.e., the subdomain over which it is nonzero is small relative to the rest of the domain. Each subdomain  $\Delta\Omega_I$  is associated with a node  $I$ . The support is often called the domain of influence of a node. The most commonly used subdomains are discs or balls. These numerical models are shown in Fig. 1. The domain is here indicated by heavy lines and lighter lines are used for the supports of the weight function. A typical node  $I$  and its support  $\Omega_I$  are also indicated. Note that there is considerable overlay of the discs (for clarity the overlap shown is considerably less than in a real computation, where 5 to 10 discs would usually overlap a point). The figure also shows the two most commonly used types of supports: discs and rectangles; although not shown here, these may be mixed in a single model.

### 2.1 Smooth Particle Hydrodynamics

**Construction** The oldest of the meshless methods is the smooth particle hydrodynamics method (SPH) (Lucy, 1977). Monaghan (1982) provided a rationale for this method by invoking the notion of a kernel approximation for  $u(\mathbf{x})$  on a domain  $\Omega$



(a) Circular.



(b) Rectangular.

Figure 1: A computational model for a meshless method showing the boundary, nodes and supports.

generated by

$$u^h(\mathbf{x}) = \int_{\Omega} w(\mathbf{x} - \mathbf{y}, h) u(\mathbf{y}) d\Omega_{\mathbf{y}}, \quad (2.1)$$

where  $u^h(\mathbf{x})$  is the approximation,  $w(\mathbf{x} - \mathbf{y}, h)$  is a *kernel* or *weight function*, and  $h$  is a measure of the size of the support; in SPH works, it is often called a *smoothing function*. According to Monaghan (1982), the kernel is required to satisfy the following conditions:

1.  $w(\mathbf{x} - \mathbf{y}, h) > 0$  on a subdomain of  $\Omega$ ,  $\Omega_I$ , (2.2a)

2.  $w(\mathbf{x} - \mathbf{y}, h) = 0$  outside the subdomain  $\Omega_I$ , (2.2b)

3. a normality property:  $\int_{\Omega} w(\mathbf{x} - \mathbf{y}, h) d\Omega = 1$ , (2.2c)

4.  $w(s, h)$  is a monotonically decreasing function, where  $s = \|\mathbf{x} - \mathbf{y}\|$ . (2.2d)

5.  $w(s, h) \rightarrow \delta(s)$  as  $h \rightarrow 0$ , where  $\delta(s)$  is the Dirac delta function. (2.2e)

The second condition is crucial to the method for it enables the approximation to be generated from a local representation, i.e.,  $u^h(\mathbf{x})$  will depend only on the values of  $u$  at nodes which are in the subdomain for which  $w(\mathbf{x} - \mathbf{y}, h)$  is nonzero. The domain over which  $w(\mathbf{x} - \mathbf{y}, h)$  is nonzero has been called the support of the weight function or its domain of influence. It is also called the window of the weight function when these methods are examined from the viewpoint of wavelets. The third condition, which is not explained in Monaghan's work, arises from consistency, although it does not assure consistency of the discrete form of the approximation. Monaghan (1982) points out that (2.1) can be viewed as the basis of an interpolation procedure and that several proofs of the convergence of interpolations use this equation as a starting point. The fifth condition seems somewhat pointless; it is hard to conceive of a realistic function whose support tends to zero that satisfies conditions 1 to 4 which does not approach the Dirac delta function, and anyway, in real computations  $h$  never approaches zero.

Three commonly used weight functions are the exponential, the cubic spline, and the quartic spline. We first consider isotropic, or polar weight functions, where the supports are circular as shown in Fig. 1a. The argument of  $w(\mathbf{x})$  is  $s = \|\mathbf{x} - \mathbf{y}\|$ ; let  $\bar{s} = s/s_{max}$ , where  $s_{max}$  is the radius of the support. Examples of weight functions

are

$$\text{exponential: } w(\bar{s}) = \begin{cases} e^{-(\bar{s}/\alpha)^2} & \text{for } \bar{s} \leq 1 \\ 0 & \text{for } \bar{s} > 1 \end{cases} \quad (2.3a)$$

$$\text{cubic spline: } w(\bar{s}) = \begin{cases} \frac{2}{3} - 4\bar{s}^2 + 4\bar{s}^3 & \text{for } \bar{s} \leq \frac{1}{2} \\ \frac{4}{3} - 4\bar{s} + 4\bar{s}^2 - \frac{4}{3}\bar{s}^3 & \text{for } \frac{1}{2} < \bar{s} \leq 1 \\ 0 & \text{for } \bar{s} > 1 \end{cases} \quad (2.3b)$$

$$\text{quartic spline: } w(\bar{s}) = \begin{cases} 1 - 6\bar{s}^2 + 8\bar{s}^3 - 3\bar{s}^4 & \text{for } \bar{s} \leq 1 \\ 0 & \text{for } \bar{s} > 1 \end{cases} \quad (2.3c)$$

For SPH, (Monaghan, 1992) uses a spline weight function in one dimension:

$$\text{SPH spline: } w(s; h) = \frac{2}{3h} \begin{cases} 1 - \frac{3}{2}q^2 + \frac{3}{4}q^3 & \text{for } q \leq 1 \\ \frac{1}{4}(2 - q)^3 & \text{for } 1 \leq q \leq 2 \\ 0 & \text{for } q \geq 2 \end{cases} \quad (2.3d)$$

where  $q = s/h$ . The exponential weight is actually  $C^{-1}$  since it is not equal to zero at  $\bar{s} = 1$ , but for numerical purposes, it resembles a weight with  $C^1$  continuity or higher; in the exponential, the parameter  $\alpha = 0.4$  results in  $w(1) \cong 0.002$ . Monaghan (1992) calls the exponential kernel the “golden rule of SPH,” but we have not found a significant advantage for the exponential over the splines, and it is computationally more demanding. The cubic, quartic, and SPH splines have been constructed to possess  $C^2$  continuity.

The supports of isotropic weight functions in convex domains are discs or balls. It is possible to generate weights also from tensor products; i.e.,

$$w(\mathbf{x} - \mathbf{x}_I) = w(x - x_I)w(y - y_I) \quad (2.4)$$

The supports of tensor-product weights are rectangular (see Fig. 1b). These weights are of advantage on regular arrangements of nodes.

For purposes of developing approximations, discrete analogs of (2.1) are needed. The discrete form of (2.1) is obtained by numerical quadrature of the right-hand side. Since the idea is to obtain a simple formula for  $u^h(\mathbf{x})$  in terms of nodal values  $u_I \equiv u(\mathbf{x}_I)$ ,  $I = 1$  to  $n_N$ , the most straightforward quadrature approaches are usually used. Thus in one dimension, the quadrature can be performed by the trapezoidal rule, which gives

$$u^h(x) = \sum_I w(x - x_I)u_I \Delta x_I, \quad (2.5)$$

where for a sequentially numbered set of nodes  $x_I$ ,  $\Delta x_I$  for interior nodes is

$$\Delta x_I = (x_{I+1} - x_{I-1})/2.$$



On the left-hand end,

$$\Delta x_{n_N-1} = (x_{I+1} - x_b)/2,$$

where  $x_b$  is the coordinate of the left boundary, with a similar expression on the right. The sum need be taken only over the points  $x_I$  where  $w(x - x_I) > 0$ .

In multi-dimensions, the quadrature is more difficult to come to grips with. Generally, formulas of the type

$$u^h(\mathbf{x}) = \sum_I w(\mathbf{x} - \mathbf{x}_I) u_I \Delta V_I \quad (2.6)$$

are used, where  $\Delta V_I$  is some measure of the domain surrounding node  $I$ . One difficulty in applying the above is the development of robust techniques for assigning  $\Delta V_I$  to each of the nodes. In SPH applications of hydrodynamics equations, the ambiguity associated with the definition of  $\Delta V_I$  can be reduced, but not eliminated, by invoking the continuity equation.

Once quadrature is performed, the approximation can then be written in a form readily recognized by people with a background in finite elements as

$$u^h(\mathbf{x}) = \sum_I \phi_I(\mathbf{x}) u_I, \quad (2.7)$$

where

$$\phi_I(\mathbf{x}) = w(\mathbf{x} - \mathbf{x}_I) \Delta V_I. \quad (2.8)$$

The functions  $\phi_I(\mathbf{x})$  are the SPH shape functions of the approximation. In most cases,  $u_I \neq u^h(\mathbf{x}_I)$ , so the parameters  $u_I$  can not be treated exactly like nodal values, and the shape functions are not true interpolants since they do not pass through the data; however, the term interpolation functions was used by us when we were unaware of this distinction and continues to be used.

The process of developing these shape functions, when first encountered by someone familiar with finite elements, is confusing. Starting with (2.1),  $u^h(\mathbf{x})$  is the approximate solution,  $u(\mathbf{y})$  the exact solution. Then  $u(\mathbf{y})$  is discretized and becomes the means of approximating  $u^h(\mathbf{x})$ . It is difficult to accept this as a rational procedure. Nevertheless, the procedure does yield shape functions (2.8) which are easily applied, and (2.1) provides theoretical insight. It is only the linkage which is fuzzy.

**Consistency** For any method to converge, it must be consistent and stable. Stability is associated with the quadrature of the Galerkin form and the character of the Galerkin procedure, which are discussed later, but consistency inherently arises from the character of the approximation. Consistency requirements depend of the order of the partial differential equations to be solved. For a partial differential equation

(PDE) of order  $2k$ , solution by a Galerkin method requires consistency of order  $k$ , i.e., a constant field for the  $k^{\text{th}}$  derivative must be represented exactly as the discretization parameter  $h$  tends to zero. For a second order PDE, this implies that consistency is satisfied if constant first derivatives must be represented exactly; for a fourth order PDE, second derivatives are represented exactly, which implies that a quadratic function must be represented exactly.

Often, consistency conditions are expressed in terms of the order of the polynomial which must be represented exactly. Thus, for second order PDEs, linear fields must be represented exactly. We will call the *order of the consistency* of an approximation the *order of the polynomial which is represented exactly*.

Consistency conditions are closely related to completeness and reproducing conditions. An approximation is complete if it provides a basis which can reproduce the function with an arbitrary order of accuracy. Since any approximation which can exactly reproduce linear polynomials can reproduce any smooth function and its first derivative with arbitrary accuracy as the approximation is refined, an approximation which has linear consistency also has linear completeness. Reproducing conditions refer to the ability of an approximation to reproduce a function if the nodal values are set by the function; thus the ability to reproduce  $n$ th order polynomials is equivalent to  $n$ th order consistency.

The continuous form of the kernel approximation (2.1) provides some insight into the effects of the consistency requirements on  $w(\mathbf{x} - \mathbf{y})$ . If constant and linear functions are to be represented exactly, then if we let  $u(\mathbf{y}) = 1$  and  $u(\mathbf{y}) = y$ , respectively, we have the requirements that (in one dimension)

$$\int_{\Omega} w(x - y) \cdot 1 dy = 1, \quad (2.9a)$$

$$\int_{\Omega} w(x - y) \cdot y dy = x. \quad (2.9b)$$

It can be seen that (2.9a) corresponds to (2.2c), so that the frequently-stated normality condition for weight functions in SPH corresponds to zeroth order consistency, or the ability to reproduce constant functions exactly, for the continuous form of SPH. To check linear consistency, we consider (2.9b). Equation (2.9b) can be elucidated by noting that (2.9a) implies

$$\int_{\Omega} w(x - y) \cdot x dy = x, \quad (2.10)$$

and subtracting (2.9b) from (2.10) gives

$$\int_{\Omega} (x - y)w(x - y)dy = 0. \quad (2.11)$$

The integral is the first moment of the weight function. The above equation is met if the function  $w(s)$  is symmetric about the origin. Therefore, once consistency is met for

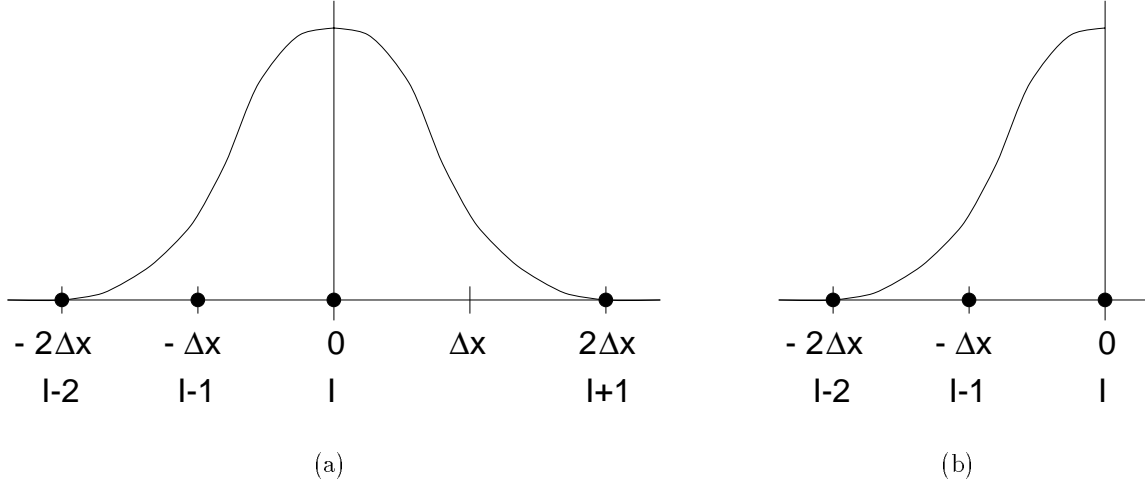


Figure 2: Illustration of linear consistency for SPH with nonuniform meshes.

the constant term, linear consistency only requires symmetry of the weight function about the origin. SPH kernels usually satisfy these conditions, so the continuous form of SPH has first order consistency.

The above conditions do not assure linear consistency for the discrete form (2.8), even in one dimension. The discrete counterpart of the consistency conditions (2.9a) and (2.11) are (in one dimension)

$$\sum_I \phi_I(x) = \sum_I \phi(x - x_I) = 1, \quad (2.12a)$$

$$\sum_I \phi_I(x)(x - x_I) = \sum_I \phi(x - x_I)(x - x_I) = 0. \quad (2.12b)$$

It can easily be shown that these consistency conditions will not be satisfied for a nonuniform arrangement of nodes. Consider, for example, the nodal arrangements shown in Fig. 2, where we consider the consistency conditions at  $x = 0$ . For the situation in Fig. 2a the consistency requirement at  $x_I$  is

$$\sum_J \phi_J(x_I)(x_J - x_I) = 0 \quad (2.13)$$

which leads to the requirement that

$$w_{I-1}\Delta V_{I-1}(-\Delta x) + w_{I+1}\Delta V_{I+1}(2\Delta x) = 0 \quad (2.14)$$

where  $\Delta V_{I-1} = \Delta x$ , and  $\Delta V_{I+1} = 2\Delta x$ . However, for a typical SPH weight function, such as the spline in (2.3d), the expression in (2.14) is equal to  $\Delta x/6$  rather than 0. Therefore, the linear consistency condition is not met.

The situation is even worse at boundaries. For the case pictured in Fig. 2b linear consistency at  $x_I$  requires that

$$w_{I-1}(x_I)\Delta V_{I-1}(-\Delta x) = 0 \quad (2.15)$$

However, that would require  $w_{I-1}(x_I)$  to vanish, which is impossible for a weight function that satisfies (2.2). Therefore linear consistency does not hold on boundaries even for uniform meshes.

It is interesting to note that in spite of the absence of linear consistency, SPH methods have provided good solutions to second order PDEs (usually posed as systems of first order PDEs). However, there have been absolutely no comparisons, as far as we know, where the spatial discretization is compared to an exact solution and the rate of convergence is checked. Linear consistency is probably not necessary for convergence (only sufficient), but this question has not been examined.

## 2.2 Moving Least Square Approximation

An alternative but related approach to developing a meshless approximation is to use a moving least square (MLS) approximation, as in Belytschko, Lu, and Gu (1994). Nayroles et al. (1992) were the first to use a moving least square procedure but developed it from the notion of diffuse elements. An excellent description of MLS is given by Lancaster and Salkauskas (1981). These approximations originate in data fitting, where it has acquired different names; in addition to MLS, local regression and loess (Cleveland, 1993) are common terms. The lowest order forms are often called Shepard functions (Shepard, 1968).

**Construction** In the moving least square approximation, we let

$$u^h(\mathbf{x}) = \sum_{i=1}^m p_i(\mathbf{x})a_i(\mathbf{x}) \equiv \mathbf{p}^T(\mathbf{x})\mathbf{a}(\mathbf{x}), \quad (2.16)$$

where  $m$  is the number of terms in the basis,  $p_i(\mathbf{x})$  are monomial basis functions, and  $a_i(\mathbf{x})$  are their coefficients, which as indicated, are functions of the spatial coordinates  $\mathbf{x}$ . Examples of commonly used bases are the linear basis:

$$\mathbf{p}^T = (1, x) \quad \text{in 1D}, \quad \mathbf{p}^T = (1, x, y) \quad \text{in 2D}, \quad (2.17a)$$

and the quadratic basis:

$$\mathbf{p}^T = (1, x, x^2) \quad \text{in 1D}, \quad \mathbf{p}^T = (1, x, y, x^2, xy, y^2) \quad \text{in 2D}. \quad (2.17b)$$

It is also possible to use other functions in a basis. For example, in problems with singular solutions, singular functions can be included in the basis. As will be

shown later, any function included in the basis can be reproduced exactly by an MLS approximation. We denote by  $k$  the highest order polynomial which is completely included in the basis.

Lancaster and Salkauskas (1981) define a local approximation by

$$u^h(\mathbf{x}, \bar{\mathbf{x}}) = \sum_{i=1}^m p_i(\bar{\mathbf{x}}) a_i(\mathbf{x}) = \mathbf{p}^T(\bar{\mathbf{x}}) \mathbf{a}(\mathbf{x}). \quad (2.18)$$

The coefficients  $a_i(\mathbf{x})$  are obtained by performing a weighted least square fit for the local approximation, which is obtained by minimizing the difference between the local approximation and the function. This yields the quadratic form

$$\begin{aligned} J &= \sum_I w(\mathbf{x} - \mathbf{x}_I) (u^h(\mathbf{x}, \mathbf{x}_I) - u(\mathbf{x}_I))^2 \\ &= \sum_I w(\mathbf{x} - \mathbf{x}_I) \left[ \sum_i p_i(\mathbf{x}_I) a_i(\mathbf{x}) - u_I \right]^2, \end{aligned} \quad (2.19)$$

where  $w(\mathbf{x} - \mathbf{x}_I)$  is a weighting function with compact support; the same weight functions as in SPH are used. Note that the term corresponding to  $u^h(\mathbf{x})$  in (2.19) consists of the monomials at  $\mathbf{x}_I$  and the coefficients at  $\mathbf{x}$ .

Equation (2.19) can be rewritten in the form

$$J = (\mathbf{P}\mathbf{a} - \mathbf{u})^T \mathbf{W}(\mathbf{x}) (\mathbf{P}\mathbf{a} - \mathbf{u}), \quad (2.20)$$

where

$$\mathbf{u}^T = (u_1, u_2 \dots u_n), \quad (2.21a)$$

$$\mathbf{P} = \begin{bmatrix} p_1(\mathbf{x}_1) & p_2(\mathbf{x}_1) & \cdots & p_m(\mathbf{x}_1) \\ p_1(\mathbf{x}_2) & p_2(\mathbf{x}_2) & \cdots & p_m(\mathbf{x}_2) \\ \vdots & \vdots & \ddots & \vdots \\ p_1(\mathbf{x}_n) & p_2(\mathbf{x}_n) & \cdots & p_m(\mathbf{x}_n) \end{bmatrix}, \quad (2.21b)$$

and

$$\mathbf{W}(\mathbf{x}) = \begin{bmatrix} w(\mathbf{x} - \mathbf{x}_1) & 0 & \cdots & 0 \\ 0 & w(\mathbf{x} - \mathbf{x}_2) & \cdots & 0 \\ \vdots & \vdots & \ddots & \vdots \\ 0 & 0 & \cdots & w(\mathbf{x} - \mathbf{x}_n) \end{bmatrix}. \quad (2.21c)$$

To find the coefficients  $\mathbf{a}(\mathbf{x})$ , we obtain the extremum of  $J$  by

$$\frac{\partial J}{\partial \mathbf{a}} = \mathbf{A}(\mathbf{x}) \mathbf{a}(\mathbf{x}) - \mathbf{B}(\mathbf{x}) \mathbf{u} = 0, \quad (2.22)$$

where  $\mathbf{A}$  is called the moment matrix and is given by

$$\mathbf{A} = \mathbf{P}^T \mathbf{W}(\mathbf{x}) \mathbf{P}, \quad (2.23a)$$

$$\mathbf{B} = \mathbf{P}^T \mathbf{W}(\mathbf{x}). \quad (2.23b)$$

So we have

$$\mathbf{a}(\mathbf{x}) = \mathbf{A}^{-1}(\mathbf{x}) \mathbf{B}(\mathbf{x}) \mathbf{u}. \quad (2.24)$$

The approximation  $u^h(\mathbf{x})$  can then be expressed as

$$u^h(\mathbf{x}) = \sum_{I=1}^n \phi_I^k(\mathbf{x}) u_I, \quad (2.25)$$

where the shape functions are given by

$$\phi^k = [\phi_1^k(\mathbf{x}) \dots \phi_n^k(\mathbf{x})] = \mathbf{p}^T(\mathbf{x}) \mathbf{A}^{-1}(\mathbf{x}) \mathbf{B}(\mathbf{x}), \quad (2.26)$$

where the superscript  $k$  is the order of the polynomial basis. The functions corresponding to  $k = 0$  are called the Shepard functions and are given by

$$\phi_I^0 = \frac{w(\mathbf{x} - \mathbf{x}_I)}{\sum_I w(\mathbf{x} - \mathbf{x}_I)}. \quad (2.27)$$

**Consistency** The demonstration of the consistency of order  $k$  of the MLS approximations is straightforward if the basis is complete in the polynomials of order  $k$ . For example, if the basis is linear, then the shape functions  $\phi^k$  will satisfy linear consistency. We follow the argument of Krongauz and Belytschko (to appear) to show consistency. Note that  $J$  in (2.19) is positive definite (with the condition (2.2a) on  $w(s)$ ). Therefore, its minimum is greater than or equal to zero. Consider a field given by

$$u(\mathbf{x}) = \sum_i \alpha_i p_i(\mathbf{x}). \quad (2.28)$$

Then if we let  $a_i(\mathbf{x}) = \alpha_i$ ,  $J$  will vanish and it will necessarily be a minimum. Thus

$$u^h(\mathbf{x}) = \sum_i \alpha_i p_i(\mathbf{x}) = u(\mathbf{x}), \quad (2.29)$$

so any function in the basis is reproduced exactly. Therefore, if the basis  $p_i(\mathbf{x})$  includes all constant and linear monomials, linear consistency is satisfied. It can similarly be shown that *any function which appears in the basis can be reproduced exactly*. This means that by including singular functions, these can be reproduced exactly; Belytschko, Krongauz, Fleming, Organ, and Liu (to appear) and Fleming, Chu, Moran, and Belytschko (1997) have used this to advantage in elastostatic fracture.

**Continuous Moving Least Square Approximations** To provide a common framework for MLS approximations and kernel approximations such as SPH and RKPM, we examine a continuous counterpart of (2.19), in the same spirit that (2.1) is the continuous counterpart of (2.5). We follow Belytschko, Gu, and Lu (1994), so we start with a weighted  $L_2$  norm, i.e. the continuous counterpart of (2.19):

$$J(\mathbf{x}) = \int_{\Omega} w(\mathbf{x} - \bar{\mathbf{x}}) [u^h(\mathbf{x}, \bar{\mathbf{x}}) - u(\bar{\mathbf{x}})]^2 d\Omega_{\bar{\mathbf{x}}}, \quad (2.30)$$

where  $w(\mathbf{x} - \bar{\mathbf{x}})$  is a weight function with compact support as in the previous developments. The approximation is taken to be of the form

$$u^h(\mathbf{x}, \bar{\mathbf{x}}) = \sum_i p_i(\bar{\mathbf{x}}) a_i(\mathbf{x}). \quad (2.31)$$

This corresponds to a local approximation in the terminology of Lancaster and Salkauskas (1981).

Minimization of (2.30) then gives

$$0 = \frac{\partial J(\mathbf{x})}{\partial a_i(\mathbf{x})} = 2 \int_{\Omega} w(\mathbf{x} - \bar{\mathbf{x}}) \left[ \sum_i p_i(\bar{\mathbf{x}}) a_i(\mathbf{x}) - u(\bar{\mathbf{x}}) \right] \sum_j p_j(\bar{\mathbf{x}}) da_j(\mathbf{x}) d\Omega_{\bar{\mathbf{x}}}. \quad (2.32)$$

Since the above must vanish for all  $da_j$ , it follows that

$$\sum_j \bar{A}_{ij}(\mathbf{x}) a_j(\mathbf{x}) = \int_{\Omega} w(\mathbf{x} - \bar{\mathbf{x}}) p_i(\bar{\mathbf{x}}) u(\bar{\mathbf{x}}) d\Omega_{\bar{\mathbf{x}}}, \quad (2.33)$$

where

$$\bar{A}_{ij}(\mathbf{x}) = \int_{\Omega} w(\mathbf{x} - \bar{\mathbf{x}}) p_i(\bar{\mathbf{x}}) p_j(\bar{\mathbf{x}}) d\Omega_{\bar{\mathbf{x}}}. \quad (2.34)$$

Note that  $\bar{\mathbf{A}}(\mathbf{x})$  is the continuous counterpart of the discrete moment matrix  $\mathbf{A}(\mathbf{x})$  as given in (2.23a). Substituting  $a_i(\mathbf{x})$  as obtained from (2.33) into (2.31) (after letting  $\mathbf{x} = \bar{\mathbf{x}}$  to obtain a global approximation) yields

$$u^h(\mathbf{x}) = \int_{\Omega} p_i(\mathbf{x}) \bar{A}_{ij}^{-1}(\mathbf{x}) p_j(\bar{\mathbf{x}}) w(\mathbf{x} - \bar{\mathbf{x}}) u(\bar{\mathbf{x}}) d\Omega_{\bar{\mathbf{x}}}. \quad (2.35)$$

The above approximation, like the discrete moving least square approximation in Section 2.2, is consistent; to prove this, use the same arguments as in Section 2.2 or see Belytschko et al. (1994). Comparison with the kernel form of SPH also reveals a striking similarity: the last two terms in (2.35) are in fact identical to the kernel form of SPH in (2.1). Thus, if the discrete form of a meshless kernel approximation can similarly be modified, it should be possible to restore consistency in discrete kernel methods. Liu et al. (1995) have called the first three terms of (2.35) a correction function: a correction of the kernel which restores consistency. In subsequent papers, Liu et al. (1995) have developed continuous and discrete forms of this correction function. In the following, a somewhat different approach is taken which leads to a simple computational procedure.

**Consistent Discrete Kernels** An alternative way to develop consistent approximations of the MLS type, which elucidates the linkage to kernel methods, is to construct  $\phi(\mathbf{x} - \mathbf{x}_I)$  so that it reproduces a group of selected functions exactly. This set of functions should include the polynomial basis for the desired order of consistency, and can also include other special functions selected for specific problems to accelerate convergence. Let the set of functions to be reproduced be  $p_i(\mathbf{x})$ . For example, for elastostatic fracture in two dimensions, Belytschko et al. (to appear) and Fleming et al. (1997) have used

$$\mathbf{p}(\mathbf{x}) = \left[ 1, x, y, \sqrt{r} \cos \frac{\theta}{2}, \sqrt{r} \sin \frac{\theta}{2}, \sqrt{r} \sin \frac{\theta}{2} \sin \theta, \sqrt{r} \cos \frac{\theta}{2} \sin \theta \right]^T. \quad (2.36)$$

The above basis satisfies linear consistency and is able to reproduce the asymptotic near-tip crack field. The condition that the shape functions  $\phi_I(\mathbf{x})$  reproduce  $p_i(\mathbf{x})$  exactly can then be written as

$$\sum_I \phi_I(\mathbf{x}) p_i(\mathbf{x}_I) = p_i(\mathbf{x}). \quad (2.37)$$

To satisfy this condition, we let

$$\phi_I(\mathbf{x}) = \sum_i \alpha_i(\mathbf{x}) p_i(\mathbf{x}_I) w_I(\mathbf{x}) = \boldsymbol{\alpha}^T(\mathbf{x}) \mathbf{p}(\mathbf{x}_I) w_I(\mathbf{x}). \quad (2.38)$$

Substituting (2.38) into (2.37) gives

$$\sum_{I=1}^n \boldsymbol{\alpha}^T(\mathbf{x}) \mathbf{p}(\mathbf{x}_I) w(\mathbf{x} - \mathbf{x}_I) p_i(\mathbf{x}_I) = p_i(\mathbf{x}). \quad (2.39)$$

This can be rewritten as

$$\mathbf{A}(\mathbf{x}) \boldsymbol{\alpha}(\mathbf{x}) = \mathbf{p}(\mathbf{x}), \quad (2.40)$$

where  $\mathbf{A}(\mathbf{x})$  is exactly the same matrix as in (2.23a). The coefficients  $\boldsymbol{\alpha}(\mathbf{x})$  can thus be found from (2.40).

To compare this form with the MLS approximation in (2.24), we substitute the expression for  $\boldsymbol{\alpha}(\mathbf{x})$  given by (2.40) into (2.38):

$$\phi_I(\mathbf{x}) = (\mathbf{A}^{-1} \mathbf{p}(\mathbf{x}))^T \mathbf{p}(\mathbf{x}_I) w(\mathbf{x} - \mathbf{x}_I) = \mathbf{p}^T(\mathbf{x}) \mathbf{A}^{-1} \mathbf{p}(\mathbf{x}_I) w(\mathbf{x} - \mathbf{x}_I) \quad (2.41)$$

where the symmetry of  $\mathbf{A}$  has been used in the last step. Comparing the last two terms in (2.41) to (2.23b), we see that

$$\phi_I(\mathbf{x}) = \mathbf{p}^T(\mathbf{x}) \mathbf{A}^{-1}(\mathbf{x}) \mathbf{B}_I(\mathbf{x}) \quad (2.42)$$



which is equivalent to (2.26).

It is essential in both this formulation and in MLS that the basis  $p_i(\mathbf{x}_I)$  consists of strongly linearly independent vectors. Otherwise, the matrix  $\mathbf{A}$  becomes poorly conditioned. This is not a problem when only a linear basis is used, provided that the governing equations are shifted to the evaluation point  $\mathbf{x}$ . The basis in (2.36) can lead to poor conditioning even at moderate distances from the crack tip because the enhancement basis and the linear basis are not strongly independent.

**Another Interpretation of Correcting for Consistency** If we strip (2.12) to its essentials, we can write the linear consistency conditions on  $\phi$  as

$$\phi \cdot \mathbf{P}_1 = 1, \quad (2.43a)$$

$$\phi \cdot \mathbf{P}_2 = 0, \quad (2.43b)$$

$$\phi \cdot \mathbf{P}_3 = 0, \quad (2.43c)$$

where

$$\phi^T = [\phi_1, \phi_2, \dots, \phi_n], \quad (2.44a)$$

$$\mathbf{P}_1^T = [p_1(\mathbf{x}_1), p_1(\mathbf{x}_2), \dots, p_1(\mathbf{x}_n)] = [1, 1, \dots, 1], \quad (2.44b)$$

$$\mathbf{P}_2^T = [p_2(\mathbf{x}_1), p_2(\mathbf{x}_2), \dots, p_2(\mathbf{x}_n)] = [x_1, x_2, \dots, x_n], \quad (2.44c)$$

$$\mathbf{P}_3^T = [p_3(\mathbf{x}_1), p_3(\mathbf{x}_2), \dots, p_3(\mathbf{x}_n)] = [y_1, y_2, \dots, y_n]. \quad (2.44d)$$

In the above, it is assumed that the origin is shifted to the point of evaluation.

Equations (2.43) are a set of three linear algebraic equations. Therefore, if  $\phi$  is expressed as a sum of any three linearly independent vectors with arbitrary coefficients, it is possible to obtain the coefficients so that consistency is satisfied by satisfying these linear equations. To satisfy linear consistency we could choose

$$\phi_I = \sum_{i=1}^3 \alpha_i(\mathbf{x}) q_i(\mathbf{x}_I) = \boldsymbol{\alpha}^T(\mathbf{x}) \mathbf{q}(\mathbf{x}_I), \quad (2.45)$$

where  $q_i(\mathbf{x})$  are three linearly independent functions. If we wish to retain the *local* character of the SPH and MLS approximations, the vectors are multiplied by  $w_I = w(\mathbf{x} - \mathbf{x}_I)$ :

$$\phi_I = \boldsymbol{\alpha}^T(\mathbf{x}) \mathbf{q}(\mathbf{x}_I) w(\mathbf{x} - \mathbf{x}_I). \quad (2.46)$$

Note that the above is a *localization of the approximation*  $\boldsymbol{\alpha}^T(\mathbf{x}) \mathbf{q}(\mathbf{x}_I)$  since  $w(\mathbf{x} - \mathbf{x}_I)$  has compact support.

To ensure the positive definiteness of the equations for  $\alpha_i$ , it is desirable to let  $\mathbf{q}(\mathbf{x}_I) = \mathbf{p}(\mathbf{x}_I)$ . Combining (2.46) with (2.43) we obtain

$$\mathbf{A} \boldsymbol{\alpha} = [1, 0, 0]^T, \quad (2.47)$$

where  $\mathbf{A}$  is the moment matrix

$$A_{ij} = \sum_{k=1}^3 w_k(\mathbf{x}) p_i(\mathbf{x}_k) p_j(\mathbf{x}_k). \quad (2.48)$$

To prove that  $\phi_I(\mathbf{x})$  computed by (2.46) is equal to  $\phi_I(\mathbf{x})$  calculated from (2.26) for the case  $\mathbf{q}(\mathbf{x}) = \mathbf{p}(\mathbf{x})$ , we note that (2.46) can be rewritten as

$$\phi(\mathbf{x}) = \boldsymbol{\alpha}^T(\mathbf{x}) \mathbf{B} \quad (2.49)$$

where

$$\phi(\mathbf{x}) = [\phi_1(\mathbf{x}), \phi_2(\mathbf{x}) \dots \phi_n(\mathbf{x})] \quad (2.50)$$

and  $\mathbf{B}$  is as in (2.23b). The consistency conditions (2.43) can be written as

$$\phi(\mathbf{x}) \mathbf{P} = \mathbf{p}^T(\mathbf{x}) \quad (2.51)$$

with  $\mathbf{P}$  as in (2.21b). Then from (2.50) and (2.51)

$$\boldsymbol{\alpha}^T \mathbf{B} \mathbf{P} = \boldsymbol{\alpha}^T \mathbf{P}^T \mathbf{W} \mathbf{P} = \boldsymbol{\alpha}^T \mathbf{A} = \mathbf{p}^T \quad (2.52)$$

with  $\mathbf{A}$  and  $\mathbf{W}$  as defined by (2.23a) and (2.21c), respectively. This proves that  $\mathbf{A}$  in (2.47) is the same as that obtained by (2.23a). Now, if we substitute  $\boldsymbol{\alpha}$  back into (2.50) we obtain

$$\phi(\mathbf{x}) = \mathbf{p}^T(\mathbf{x}) \mathbf{A}^{-1} \mathbf{B} \quad (2.53)$$

i.e., the expressions for shape functions are the same for a basis of any order.

Thus if we choose the same parent weight function, or kernel, for a kernel method such as SPH and impose the consistency requirement of order  $k$ , the resulting shape function is identical to the MLS approximation of order  $k$ . As in MLS, the kernels can also be designed to reproduce functions other than the polynomial basis.

It is possible to interpret (2.43) in yet another manner. Note that if

$$\phi_I = \alpha_I(\mathbf{x}) w_I(\mathbf{x}) \quad (\text{no sum on } I) \quad (2.54)$$

then solving (2.43) is equivalent to:

1. finding  $\boldsymbol{\alpha}$  such that  $\boldsymbol{\alpha}$  is orthogonal to  $\mathbf{P}_2$  and  $\mathbf{P}_3$  under the dot product

$$\mathbf{a} \cdot \mathbf{b} = \sum_{I=1}^n w_I a_I b_I; \quad (2.55)$$

2. scaling  $\phi$  to satisfy (2.43a).

Step 1 can be accomplished by the Gram-Schmidt procedure. It can be shown that if we use  $\mathbf{1}$  as the starting vector for Gram-Schmidt, then the shape functions will be the same as those obtained in (2.26) with a linear basis.

## 2.3 Partition of Unity Methods

Meshless methods can also be based on partitions of unity. This viewpoint has been advanced by Duarte and Oden (1996) and Babuška and Melenk (1995).

A partition of unity is a paradigm in which a domain is covered by overlapping patches, or subdomains  $\Omega_I$ , each of which is associated with a function  $\phi_I(\mathbf{x})$  which is nonzero only in  $\Omega_I$  and has the property that

$$\sum_I \phi_I(\mathbf{x}) = 1 \text{ in } \Omega. \quad (2.56)$$

(Note the similarity to Fig. 1 and associated text.) In addition, Duarte and Oden (1996) state the property that  $\phi_I(\mathbf{x}) \in C^\infty$ , but this property is not essential in constructing meshless approximations. Partitions of unity are widely used in mathematics to construct proofs on nonlinear manifolds.

The essential condition of a partition of unity (2.56) is identical to the zeroth order consistency condition (2.12a). Thus the construction of a partition of unity is identical to the construction of the weight function or consistent kernel in a meshless approximation. In particular, the MLS functions  $\phi^0(\mathbf{x}) = w(\mathbf{x} - \mathbf{x}_I) / \sum_I w(\mathbf{x} - \mathbf{x}_I)$ , i.e., the Shepard functions, and  $\phi^k(\mathbf{x})$  for any  $k$  are partitions of unity. To see the latter, recall that by consistency,

$$\sum_I \phi_I^k(\mathbf{x}) x_I^p = x^p, \text{ for } 0 \leq p \leq k. \quad (2.57)$$

Hence, if  $p = 0$ ,

$$\sum_I \phi_I^k(\mathbf{x}) \cdot 1 = \sum_I \phi_I^k(\mathbf{x}) = 1. \quad (2.58)$$

This viewpoint has led to several new approximations for meshless methods. Babuška and Melenk (1995) have developed a method they call the partition of unity finite element method (PUFEM). For the Helmholtz equation in one dimension, they introduce approximations of the form

$$u^h(x) = \sum_I \phi_I^0(x) (a_{0I} + a_{1I}x + \dots + a_{kI}x^k + b_{1I} \sinh nx + b_{2I} \cosh nx) \quad (2.59)$$

We can write the above as

$$u^h(x) = \sum_I \phi_I^0(x) \sum_i \beta_{iI} p_i(x) \quad (2.60)$$

where

$$\begin{aligned} \beta_{iI} &= [a_{0I}, a_{1I}, \dots, a_{kI}, b_{1I}, b_{2I}] \\ \mathbf{p}^T &= [1, x, \dots, x^k, \sinh nx, \cosh nx] \end{aligned}$$

Here,  $\phi^0(x)$  is the Shepard function, or the zeroth order MLS approximation, which provides the partition of unity and hence the compact support of the approximation. The coefficients  $a_{1I}, \dots, a_{kI}, b_{1I}, b_{2I}$  are the unknowns of the approximation and can be determined by a Galerkin or collocation procedure. The degree of consistency depends on the number of terms  $x^k$ : for linear consistency in one dimension, two unknowns are needed at each node. The functions  $\cosh nx$  and  $\sinh nx$  are enhancement functions similar to the enhancement functions in (2.36) but *extrinsic* to the basis which improve the accuracy for this particular equation; the use of two extrinsic basis functions leads to two additional unknowns per node. Note that this method requires at least two unknowns per node (without the enhancement) to attain linear consistency, whereas an MLS approximation of order 2 requires only one unknown per node for linear consistency. In computations,  $p_i(x)$  is generally replaced by  $p_i(x - x_I)$  for better conditioning.

Babuška and Melenk also introduce the approximation

$$\begin{aligned} u^h(x) &= \sum_J \phi_J^0(x) \sum_I b_I L_{JI}(x) \\ &= \sum_I \sum_{J: x_I \in \Omega_J} \phi_J^0(x) L_{JI}(x) b_I \end{aligned} \quad (2.61)$$

where  $L_{JI}(x)$  are the Lagrange interpolants, so that  $L_{JI}(x_K) = \delta_{IK}$  for any  $J$ , and  $a_I$  is the approximation value associated with node  $I$ .

We prove that PUFEM shape function based on Lagrange polynomials satisfy the Kronecker delta condition

$$\phi_I(x_J) = \delta_{IJ} \quad (2.62)$$

in the following manner. Let  $J$  denote the patch number ( $\Omega_J$ ) and let each patch have  $p + 1$  Lagrange interpolation points  $x_I$ . (This is tricky in two and three dimensions unless you have elements.) Then let us denote by  $L_{JI}$  the Lagrange polynomial of degree  $p$  in patch  $J$  that is 1 at  $x_I$ . Then, since

$$\phi_I(x) = \sum_{J: x_I \in \Omega_J} \phi_J^0(x) L_{JI}(x) \quad (2.63)$$

we have

$$\phi_I(x_K) = \sum_{J: x_I \in \Omega_J} \phi_J^0(x_K) L_{JI}(x_K) = \sum_{J: x_I \in \Omega_J} \phi_J^0(x_K) \delta_{IK} = \delta_{IK} \quad (2.64)$$

since

$$\sum_I \phi_I^0(x) = 1 \quad (2.65)$$

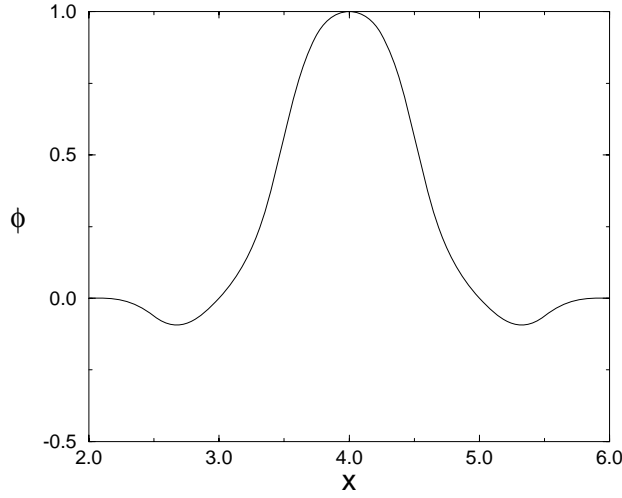


Figure 3: PUFEM shape function

and

$$L_{JI}(x_K) = \delta_{IK} \quad (2.66)$$

A plot of a sample shape function for second order Lagrange polynomials using quartic weight function with  $s_{max} = h$  is shown in Fig. 3. The extension to a meshless method in multi-dimensions does not seem easy because in the construction of the Lagrange interpolant, an ordering of the nodes in all directions must be known.

Duarte and Oden (1996) use the partition of unity concept in a more general manner by constructing it from an MLS shape function of order  $k$ ; they call the method *hp* clouds. In our notation, their approximation is

$$u^h(x) = \sum_I \phi_I^k(x) \left( u_I + \sum_{i=1}^m b_{iI} q_i(x) \right) \quad (2.67)$$

Here  $q_i(x)$  can be a monomial basis of any order greater than  $k$ . To improve conditioning, they express the higher order terms using Legendre polynomials. The functions  $q_j(x)$  are either higher order monomials or are enhancement functions; we call this the extrinsic basis.

The major advantage of the Duarte-Oden formulation is that it enables the extrinsic basis to vary from node to node, thus facilitating *hp*-adaptivity. The concept of an extrinsic basis is essential for obtaining *p*-adaptivity. In MLS approximations, the intrinsic basis, and hence the order of the polynomial, cannot be changed without introducing a discontinuity, i.e., if we examine (2.16) we see that unless  $a_i(\mathbf{x})$  fortuitously vanishes along some line,  $p_i(\mathbf{x})$  cannot be dropped from the intrinsic basis.

On the other hand, the extrinsic basis can be adjusted arbitrarily, so extra terms can be added arbitrarily at any nodes without violating continuity.

An extension of this approach is to use different partitions of unity for the enhancement. A particularly useful form of this approximation is

$$u^h(x) = \sum_{I=1}^{n_1} \phi_I^k u_I + \sum_{I=1}^{n_2} \phi_I^0 \sum_i b_{iI} q_i(x) \quad (2.68)$$

where  $q_i(x)$  are usually enhancement functions, such as the singular functions associated with a crack tip. Generally  $n_2 \ll n_1$ , since the coefficients of the enhancement functions vary little over the domain. The goal in this construction is to decrease the linear dependence of  $u_I$  and  $b_{iI}$  by using different partitions of unity. The linear dependence can be decreased by using different nodes and supports for  $\phi_I^k(\mathbf{x})$  and  $\phi_I^0(\mathbf{x})$ ; for example, alternate nodes can be used for  $\phi_I^0$  with a larger domain of influence.

A different way of constructing meshless approximations is to directly determine all derivatives at a node. One method of this type is the generalized finite difference method, which was developed by Liszka and Orkisz (1980). Details of this method are developed in a companion paper in this volume.

## 2.4 Summary

A summary of the approximations based on kernels or partitions of unity is given in Table 1. We have shown two forms of the approximations: the discrete form, and where applicable, the continuous form. The continuous form does not play a direct role in the numerics; its main role is its linkage to the theoretical frameworks provided by kernel approximation theory and wavelets; the latter is under study by Liu and coworkers (Liu and Chen, 1995; Liu et al., 1996).

The interrelationships of these developments can also be expressed as shown in Fig. 4. The taxonomy consists basically of two columns: moving least square approximations and kernel approximations. As has been shown in the preceding, when consistency is introduced in a parent kernel by a basis  $\mathbf{p}(\mathbf{x})$ , a consistent kernel approximation is equivalent to the MLS approximation if the weight function is the same as the parent kernel and the intrinsic basis is the same. Underlying the two methods is the concept of the partition of unity; it provides a rational method for constructing localized approximations to global functions with a greater degree of flexibility.

## 3 Discontinuities in Approximations

The emphasis in the construction of meshless approximations based on partitions of unity or MLS has up to this time been placed on simple domains, such as rectangles and simply connected bodies, with constant or smoothly varying parameters in the governing equations. However, many practical problems involve multiply connected

Method	Discrete Form	Continuous Form
Smooth Particle Hydrodynamics (SPH), Kernel Method	$u^h(\mathbf{x}) = \sum_I N_I(\mathbf{x})u_I$	$u^h(\mathbf{x}) = \int_{\Omega} w(\mathbf{x} - \mathbf{y})u(\mathbf{y})d\Omega_{\mathbf{y}}$ Monaghan (1982)
Moving Least Square Approximation	$u^h(\mathbf{x}) = \mathbf{p}^T(\mathbf{x})\mathbf{a}(\mathbf{x})$ $N_I(\mathbf{x}) = \mathbf{p}^T(\mathbf{x})\mathbf{D}(\mathbf{x})$ Nayroles et al. (1992) Belytschko et al. (1994)	$u^h(\mathbf{x}) = \int_{\Omega} C(\mathbf{x}, \bar{\mathbf{x}})w(\mathbf{x} - \bar{\mathbf{x}})u(\bar{\mathbf{x}})d\Omega_{\bar{\mathbf{x}}}$ Belytschko et al. (1994)
Reproducing Kernel Methods	$N_I = \mathbf{a}^T \mathbf{p}(\mathbf{x} - \mathbf{x}_I)w(\mathbf{x} - \mathbf{x}_I)$ $= \mathbf{p}^T \mathbf{D}(\mathbf{x})$ Liu et al. (1995)	$u^h(\mathbf{x}) = \int_{\Omega} C(\mathbf{x}, \mathbf{y})w(\mathbf{x} - \mathbf{y})u(\mathbf{y})d\Omega_{\mathbf{y}}$ Liu et al. (1995)
$H_p$ clouds	$N_I = \phi_I^k(u_I + \mathbf{b}_I^T \mathbf{p}(\mathbf{x}))$ Duarte and Oden (1996)	
PUFEM	$N_I = \phi_I^0(u_I + \mathbf{b}_I^T \mathbf{p}(\mathbf{x}))$ Babuška and Melenk (1995)	

Table 1: Selected Meshless Approximation Functions and their Continuous Counterparts.

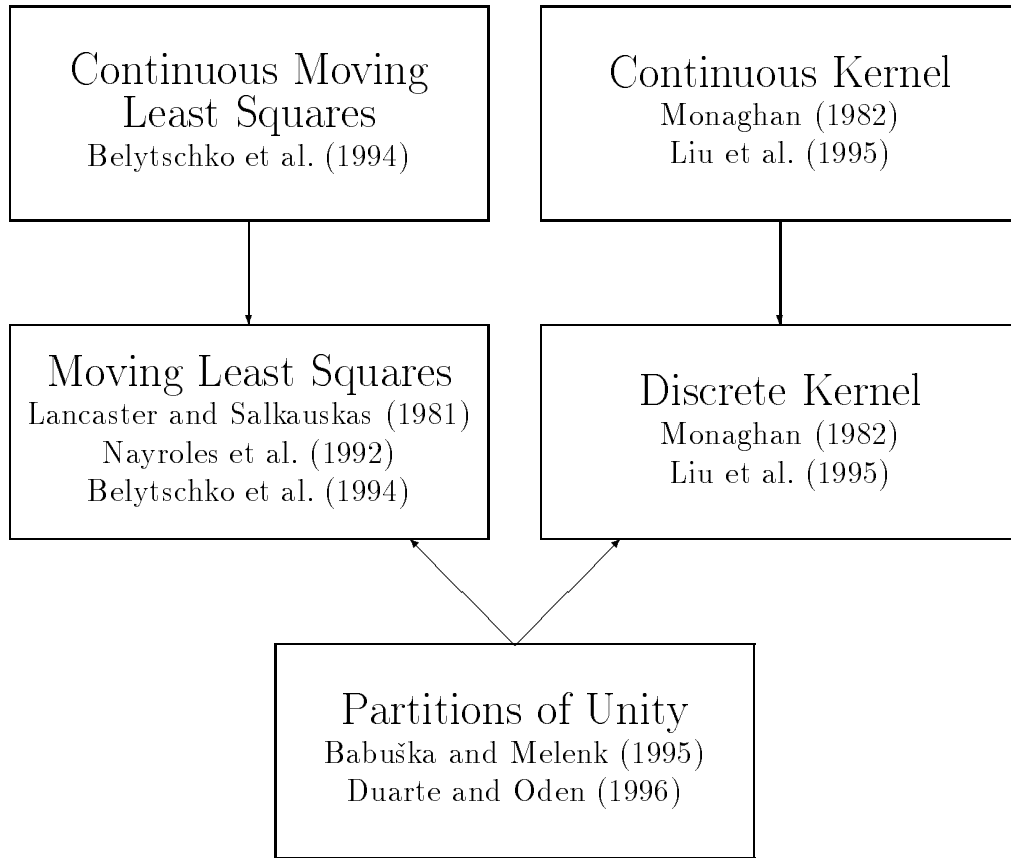


Figure 4: Interrelationship of meshless approximation methods and paradigms.



domains and various discontinuities in the solutions or their derivatives. Moreover, in many technically important problems, we encounter singular solutions.

While the high order of continuity which MLS meshless methods inherit from the weight function can be considered a blessing because it provides solutions with smooth derivatives, it can also be a disadvantage in problems where the coefficients of the PDE are discontinuous. For example, in elastostatics, problems involving two materials (i.e., where the coefficients in the PDE are discontinuous along the interface between the materials) result in solutions with discontinuous derivatives along the interface. When the approximation is a smooth function such as MLS, the discontinuity in the derivatives introduces spurious oscillations. Similarly, when a crack is modeled in a body, the dependent variables, i.e., the displacements, must be discontinuous across the crack. The introduction of discontinuities also requires special techniques in meshless methods based on moving least squares and in partitions of unity.

### 3.1 Visibility Criterion for Discontinuous Approximations

The simplest way to introduce discontinuities into meshless approximations is to use the visibility criterion in their construction (Belytschko, Lu, and Gu (1994); the name was coined in Krysl and Belytschko (to appear)). In this approach, the boundaries of the body and any interior lines of discontinuity are considered opaque when constructing the weight functions. By opacity, we mean that when the domain of influence for the weight function is constructed, the line from a point to a node is imagined to be a ray of light. If the ray encounters an opaque surface, such as the boundary of a body or an interior discontinuity, it is terminated and the point is not included in the domain of influence.

For example, if we consider a crack, i.e., a line of discontinuity in the displacements which terminates at the crack tip, the domain of influence of a generic node  $I$  in the vicinity of the crack tip takes the shape shown in Fig. 5 when the visibility criterion is used. Points in the shaded region of the original domain of influence are removed from the domain of influence because the rays from points in the shaded domain to  $\mathbf{x}_I$  cross the line of discontinuity.

A consequence of the visibility criterion is that a discontinuity is introduced into the weight function and shape function wherever the domain of influence is cut by a line of discontinuity. Contour plots for the weight functions and shape functions of nodes  $I$  and  $J$  are shown in Fig. 6. As can be seen from the contour plots, the weight function of node  $J$  and its shape function are discontinuous along the specified line, so the visibility criterion is effective in introducing the desired discontinuity.

However, for a shape function near the tip of the line of discontinuity, a byproduct of the visibility criterion is a discontinuity in the approximation within the domain. Along the ray which grazes the tip of the discontinuity, line AB in Fig. 5, the weight function is nonzero at all points except B to the right of the line, but vanishes to the left. Thus the weight function is discontinuous, which can also be seen from the

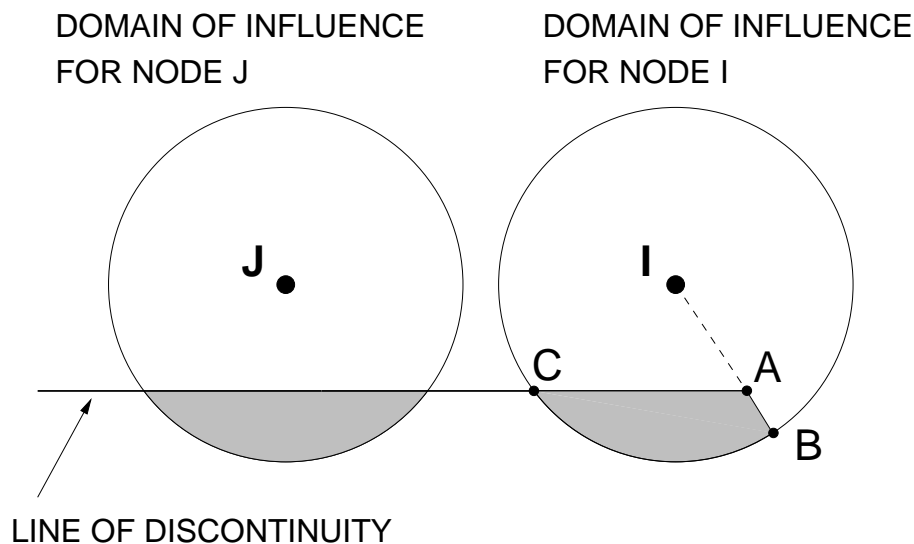


Figure 5: Domains of influence of nodes adjacent to a line of discontinuity for the visibility criterion; the shaded regions are removed from the domain of influence.

contour plots of Fig. 6. The surface plots of the shape function, Fig. 7, show that this introduces a discontinuity along the line AB. Moreover, additional discontinuities are introduced in the shape functions by the discontinuities in the weight functions of other nodes near the tip of the discontinuity. As a consequence, the approximation will not be continuous within the domain, which is undesirable in a Galerkin method. It should be mentioned that these discontinuities do not lead to failure of convergence. Krysl and Belytschko (to appear) have shown that the resulting approximations can lead to convergent solutions.

The visibility test also leads to difficulties along nonconvex boundaries. For example, consider a line of discontinuity which is nonconvex as shown in Fig. 8. On the convex side, node  $J$ , the boundaries of the domain of influence correspond to the line of discontinuity, so the weight function and shape function are discontinuous only where desired. However, for node  $I$ , part of the boundary of the domain of influence is interior to the smooth domain, so discontinuities will result in the approximation.

### 3.2 Diffraction Method for Discontinuous Functions

Belytschko et al. (to appear) and Organ et al. (1996) have described a method for construction of approximations around the tip of a discontinuity called the *diffraction method*. The method is motivated by the way light diffracts around a sharp corner, but the equations used in constructing the domain of influence and the weight function bear almost no relationship to the equations of diffraction.

Consider the end of a line of discontinuity as shown in Fig. 5. The technique

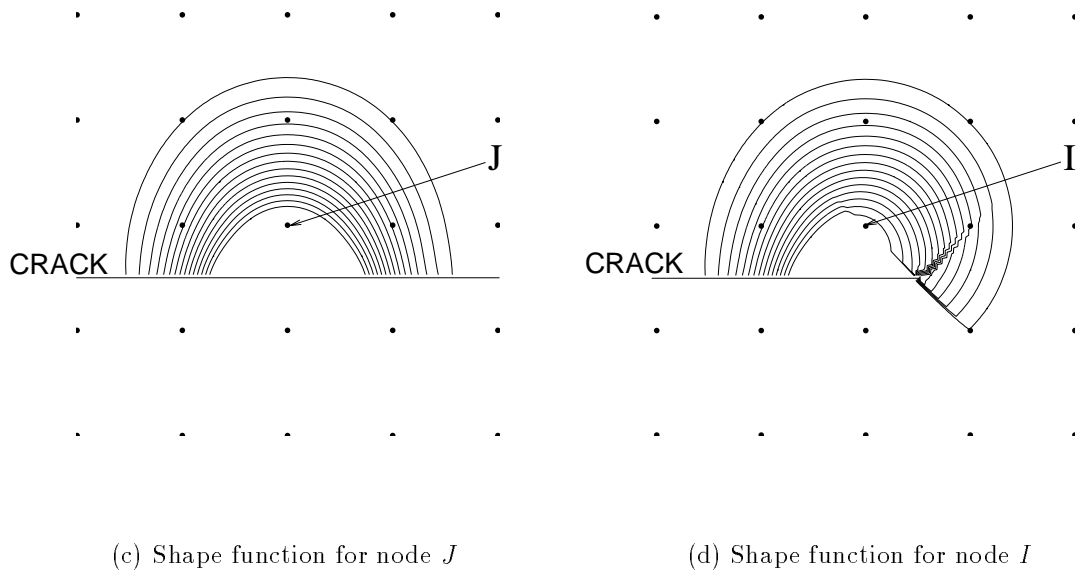
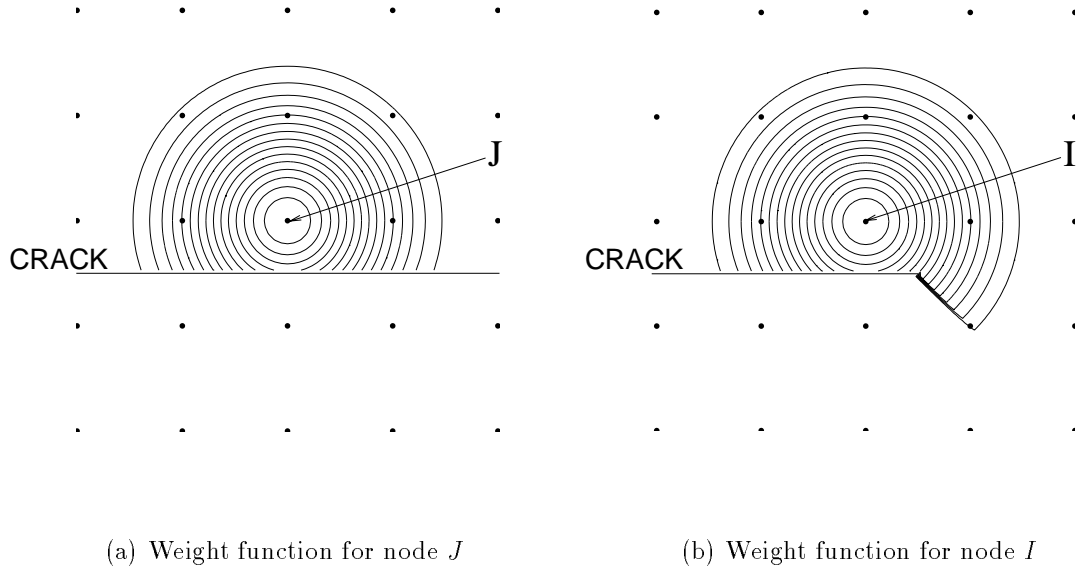


Figure 6: Contour plots of the weight function  $w(\mathbf{x} - \mathbf{x}_I)$  and shape function  $\phi_I(\mathbf{x})$  as determined by the visibility criterion for nodes adjacent to a line of discontinuity due to a crack.

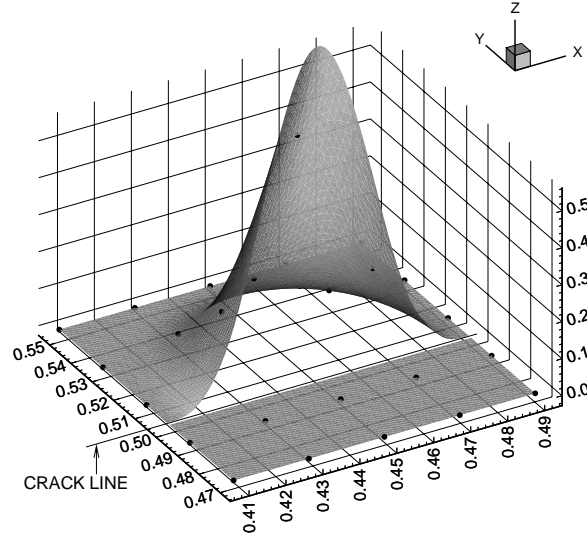
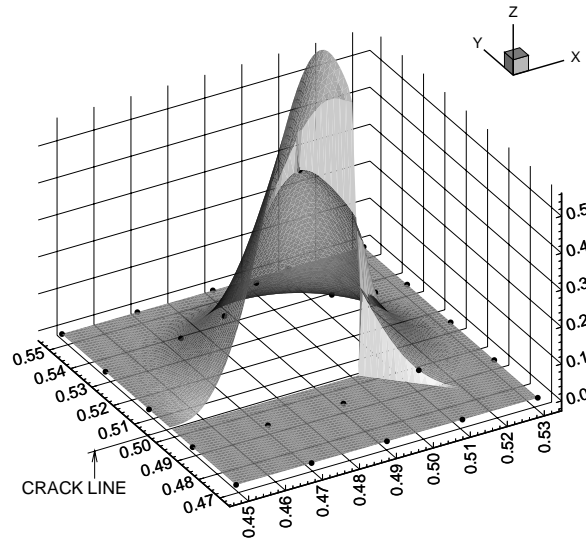
(a) Shape function for node  $J$ (b) Shape function for node  $I$ 

Figure 7: Shape functions as determined by the visibility criterion for nodes near a line of discontinuity due to a crack.

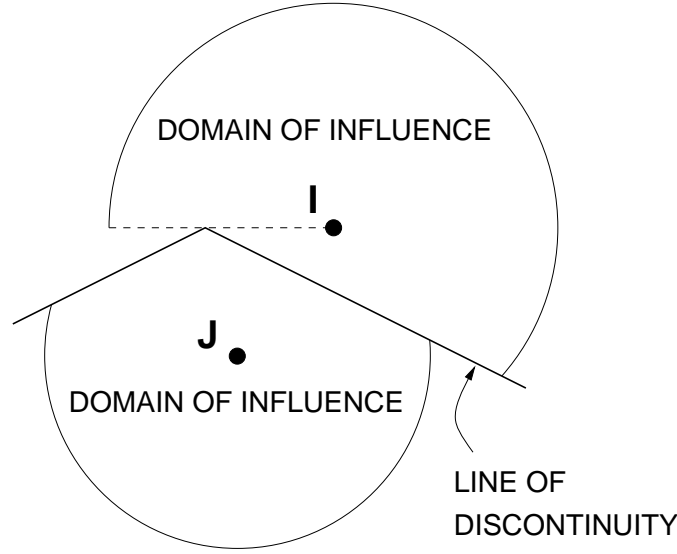


Figure 8: Domains of influence for nodes near a nonconvex line of discontinuity as determined by the visibility criterion.

described here applies only to polar-type weights where the weight function is defined as a function of a single parameter  $s$ ; the same weight functions as in Section 2.1 can be used. Moreover, for reasons to be described shortly, we define the domain of influence of node  $I$  by the condition that  $w(s) > 0$  in  $\Omega_I$ .

The essence of the diffraction method is to treat the line of discontinuity as opaque but to evaluate the length of the ray  $s$  by a path which passes around the corner of the discontinuity. This is illustrated in Fig. 9, which shows a typical point which would not lie within the domain of influence if the visibility criterion is used. The weight parameter  $s$  is computed by

$$s(\mathbf{x}) = \left( \frac{s_1 + s_2(\mathbf{x})}{s_0(\mathbf{x})} \right)^\lambda s_0(\mathbf{x}), \quad (3.1)$$

where

$$s_0(\mathbf{x}) = \|\mathbf{x} - \mathbf{x}_I\|, \quad s_1 = \|\mathbf{x}_c - \mathbf{x}_I\|, \quad s_2(\mathbf{x}) = \|\mathbf{x} - \mathbf{x}_c\|. \quad (3.2)$$

As a result, the domain of influence as given by the criterion  $w_I(s) = 0$  contracts on the far side of the discontinuity as shown in Fig. 10. Thus the domain of influence is determined by the condition that the weight function vanishes.

Contour plots of the weight function and shape function are shown in Fig. 11. As can be seen, both the weight function and shape function are continuous within the domain but are discontinuous across the specified line. The derivative of the shape function is multiple valued at the tip of the discontinuity but this should cause no

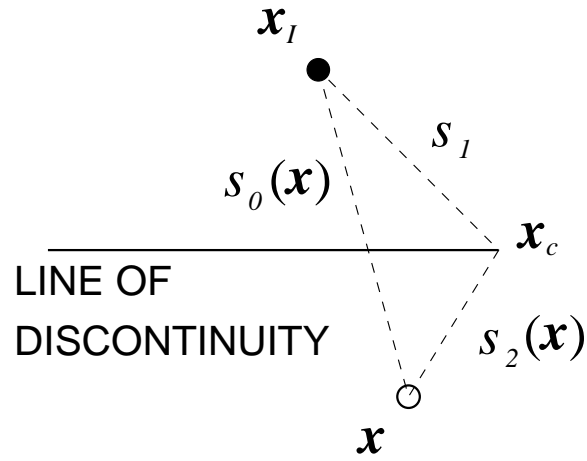


Figure 9: Scheme for the diffraction method for a node near the tip of a line of discontinuity.

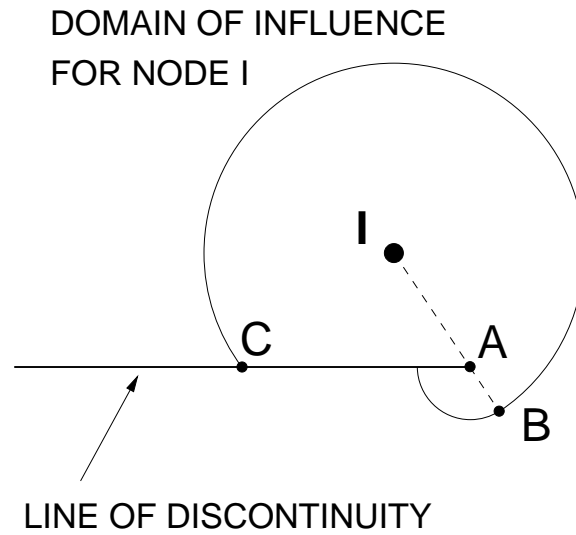


Figure 10: Domain of influence of a weight function by the diffraction method near a line of discontinuity.

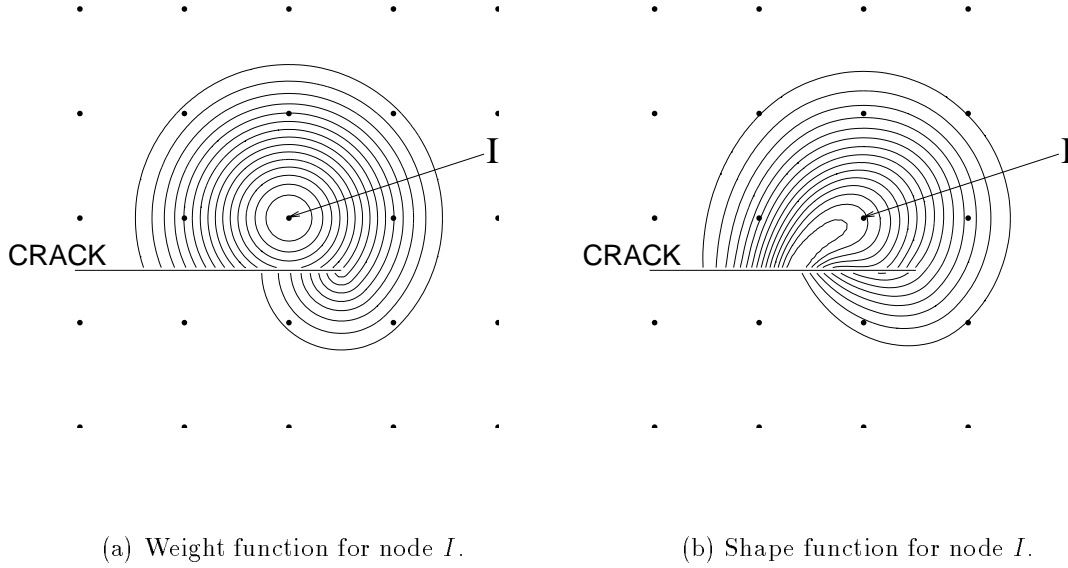


Figure 11: Contour plots of weight and shape functions by the diffraction method.

difficulties. Thus a Galerkin method can be used with these shape functions without committing any variational crimes.

The shape function for this node is shown in Fig. 12. Again, the smoothness of the shape function within the domain is quite apparent. It should be noted, however, that the shape function is quite complex with several areas of rapidly varying derivatives, so quadrature of the discrete Galerkin forms can present difficulties.

The diffraction method can also be used on nonconvex boundaries of multiply connected bodies. The procedure is demonstrated in Fig. 13, where the parameter  $s$  for points invisible through the opaque boundaries is constructed from the lengths of two line segments which just graze the boundary.

The extension of the diffraction method to three dimensions is somewhat more difficult. The analytical forms of the derivatives are quite cumbersome and we have chosen to evaluate the derivatives numerically in this case. Also, for nonconvex boundaries such as holes, the need for these modifications is not clear in instances when the visibility criterion is not adhered to.

Duarte (1996) has suggested a *continuous line criterion* where any point which can be joined with the generating node of the original domain of influence remains in the domain. This criterion is simple and effective for holes and nonconvex boundaries.

These techniques are applicable to any methods based on kernels, partitions of unity or MLS, for in all of these methods the continuity of the kernel (weight function)

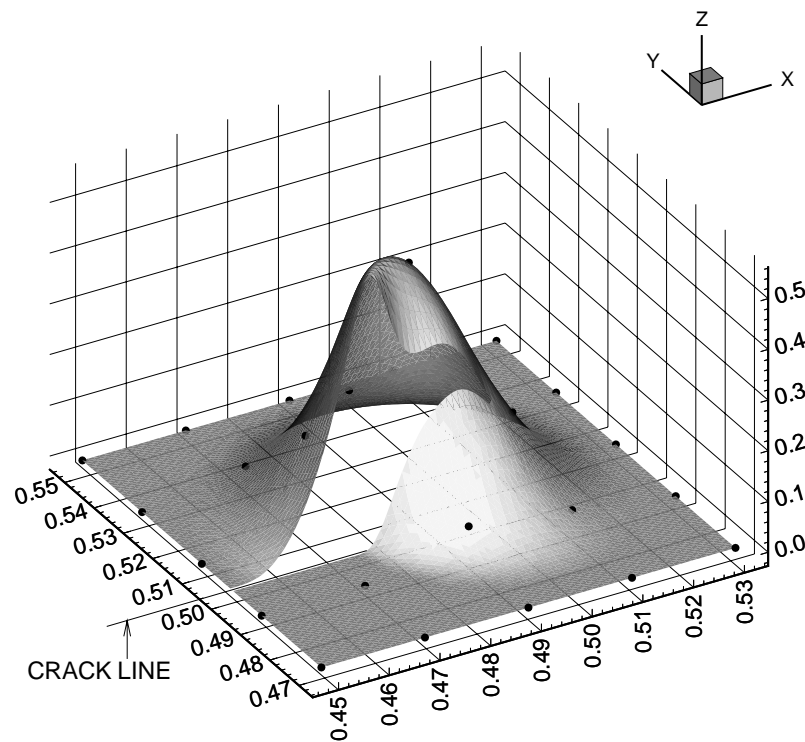


Figure 12: Surface plot of the shape function for node  $I$  by the diffraction method.



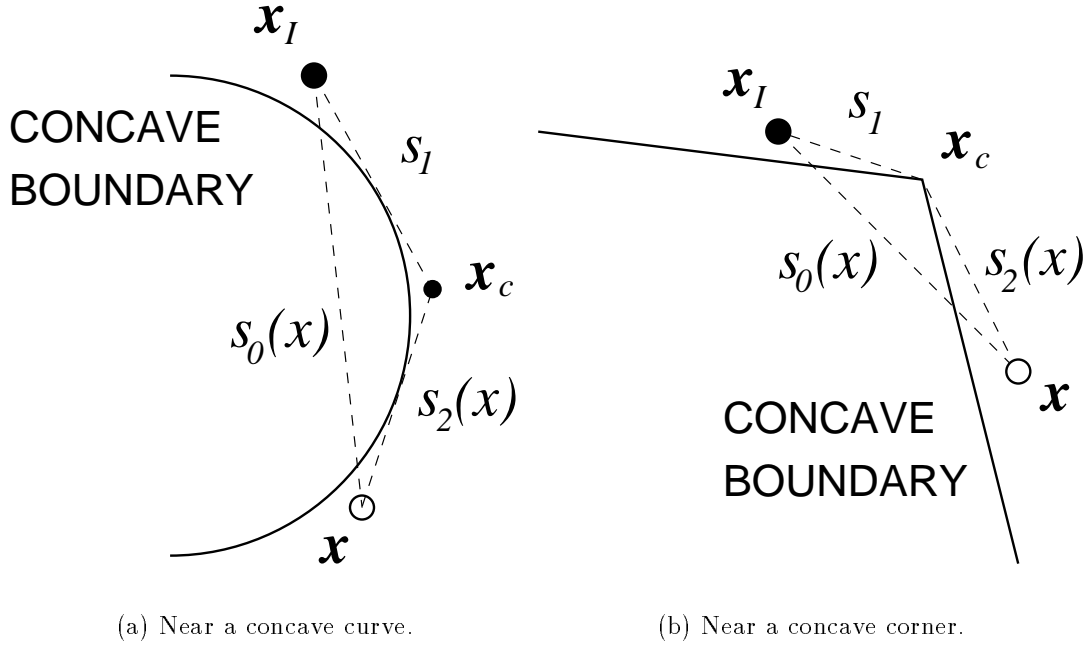


Figure 13: The diffraction method near different types of nonconvex boundaries.

determines the continuity of the approximation. It is not applicable to SPH in its present form because boundaries are not explicitly defined and fracture appears to be modeled by simply separating the nodes far enough so that the domains of influence of nodes across the discontinuity no longer interact.

### 3.3 Transparency Method for Discontinuous Functions

In the *transparency method* (Organ et al., 1996), the function is smoothed around the tip of a discontinuity by endowing the surface, or line, of discontinuity with a varying degree of transparency. At the tip, the line of discontinuity is considered completely transparent, and the transparency diminishes as we move away from the tip of the discontinuity. When a ray from the evaluation point  $\mathbf{x}$  to the node  $\mathbf{x}_I$  intersects a line of discontinuity, the parameter  $s$  is modified (lengthened) by

$$s(\mathbf{x}) = s_0(\mathbf{x}) + s_{max} \left( \frac{s_c(\mathbf{x})}{\bar{s}_c} \right)^\lambda, \quad \lambda \geq 2, \quad (3.3)$$

where  $s_0(\mathbf{x})$  is defined in (3.2),  $s_{max}$  is the radius of the nodal support, and  $s_c(\mathbf{x})$  is the distance from the crack tip to the intersection point (see Fig. 14). The parameter  $\bar{s}_c$  sets the intersection distance at which the crack segment is completely opaque:

$$\bar{s}_c = \kappa h, \quad (3.4)$$

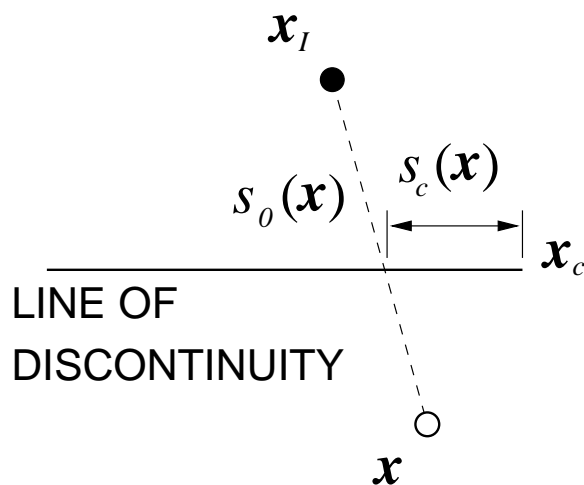


Figure 14: Computation of support radius for transparency method.

where the parameter  $\kappa$  is used to vary the opacity, and  $h$  is a measure of nodal spacing. Fig. 15 shows a surface plot of the weight function near the tip of a discontinuity using the transparency method. It should be noted that because the second term in (3.3) is at least quadratic, the shape function and its derivatives are continuous at the crack tip. As in the diffraction method, the domain of influence is determined by the condition  $w(s) \geq 0$ .

An additional requirement has been added to this method to account for cases where nodes are very close to the crack. For nodes adjacent to a boundary, the angle between the crack and the ray from the node to the crack tip is small, causing a sharp gradient in the weight function across the line ahead of the crack. Therefore, we require that all nodes be a minimum distance from the crack surface, i.e., the normal distance to the crack surface must be larger than  $\gamma h$ , where  $0 < \gamma < 1$ ;  $\gamma$  is usually about  $1/4$ .

### 3.4 Discontinuous Derivatives

When the coefficients of PDEs are discontinuous functions of the spatial variables, the solutions usually have discontinuous derivatives along the same lines and surfaces in two and three dimensions, respectively. For example, in elastostatic problems with multiple materials, the derivatives of the displacements are discontinuous across the material interfaces. In finite element methods, these discontinuities are introduced quite naturally by placing element boundaries along the material interface. Since meshless methods lack element interfaces, the possibility of discontinuous derivatives must be treated differently.

Cordes and Moran (submitted) have treated discontinuous derivatives by a Lagrange multiplier technique. The approximations are disjoint across the interface,

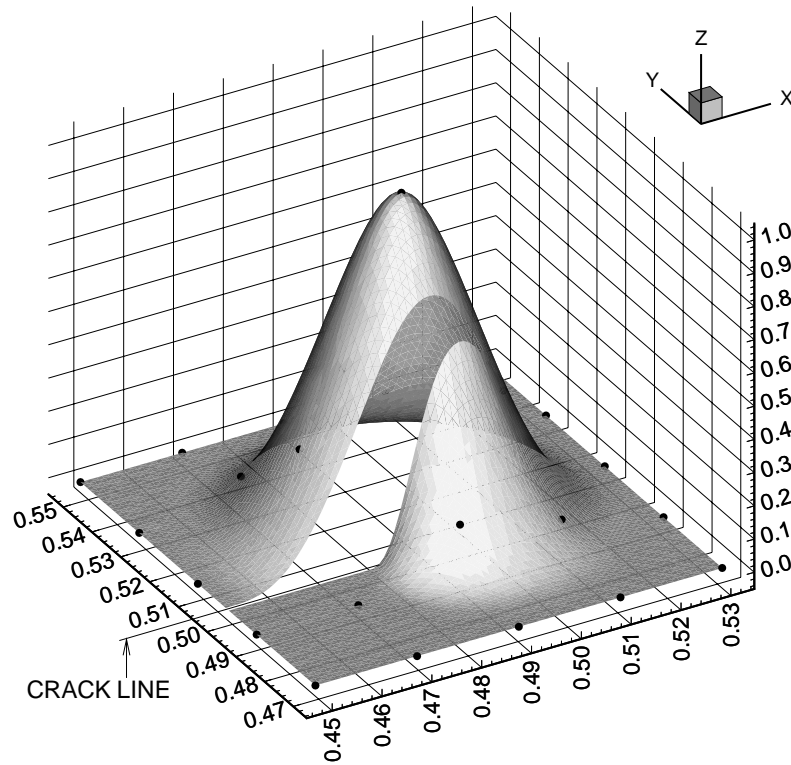


Figure 15: Surface plot of a weight function for node  $I$  by the transparency method.

and continuity is imposed by Lagrange multipliers.

Krongauz and Belytschko (submitted,b) have developed several techniques for introducing discontinuous derivatives into the solution. We will here describe two of the methods, beginning with the one-dimensional case. Suppose we have the possibility of a discontinuity at the point  $x = x_a$ . The approximation is then taken to be

$$u^h(x) = \sum_I \phi_I^k(x) u_I + b \Psi(x - x_a) \quad (3.5)$$

where  $\Psi(x - x_a)$  is the function which generates the discontinuous derivative and  $b$  is its strength, which is an unknown in the Galerkin procedure;  $\Psi(x)$  is called the jump term.

For computational efficiency and robustness,  $\Psi(x - x_a)$  should have compact support, be linearly independent of the MLS basis of the first term in (3.5) and for purposes of rapid convergence, should be able to reproduce a derivative which is a Heaviside step function. Two forms have been developed; the first is

$$\Psi(\bar{r}) = \begin{cases} -\frac{1}{6}\bar{r}^3 + \frac{1}{2}\bar{r}^2 - \frac{1}{2}\bar{r} + \frac{1}{6} & \bar{r} \leq 1 \\ 0 & \bar{r} \geq 1 \end{cases} \quad (3.6)$$

where  $\bar{r} = |x - x_a|/r_{max}$ . The second form is

$$\Psi(x) = \langle x - x_a \rangle - \sum_I \phi_I(x) \langle x_I - x_a \rangle \quad (3.7)$$

where the function  $\langle x \rangle$  is

$$\langle x \rangle = \begin{cases} 0 & x < 0 \\ x & x \geq 0 \end{cases} \quad (3.8)$$

The two functions are shown in Fig 16. The first has the advantage that it can exactly interpolate a function which has the derivative in the form of a Heaviside step function, but when extended to two dimensions it will not have compact support and will need a special modification to regain it.

In two dimensions, the approximation becomes

$$u^h(\mathbf{x}) = \sum_I \phi_I(\mathbf{x}) u_I + b(s) \Psi(r) = \sum_I \phi_I(\mathbf{x}) u_I + \sum_J b_J N_J(s) \Psi(r) \quad (3.9)$$

where  $N_J(s)$  are one dimensional shape functions expressed in terms of the arc length of the line and  $b_J$  are nodal parameters governing the strength of the discontinuity. The construction is illustrated in Fig 17. which shows the nodes that are placed along the line of derivative discontinuity.

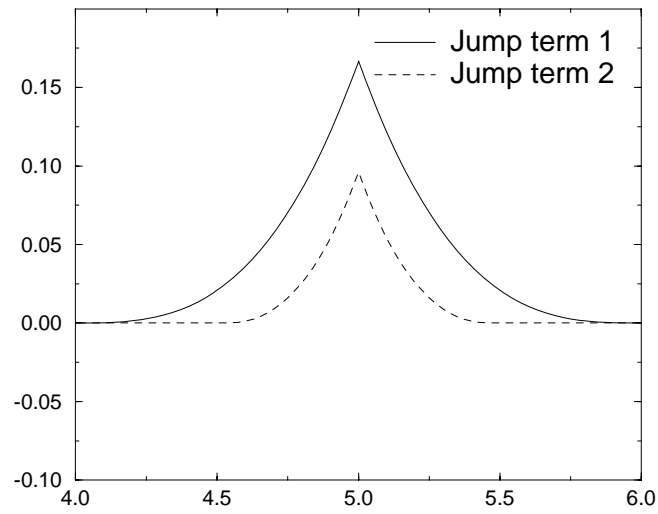
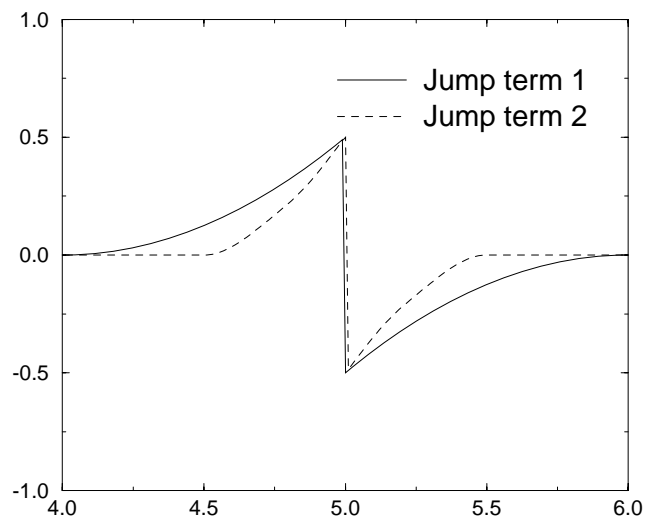
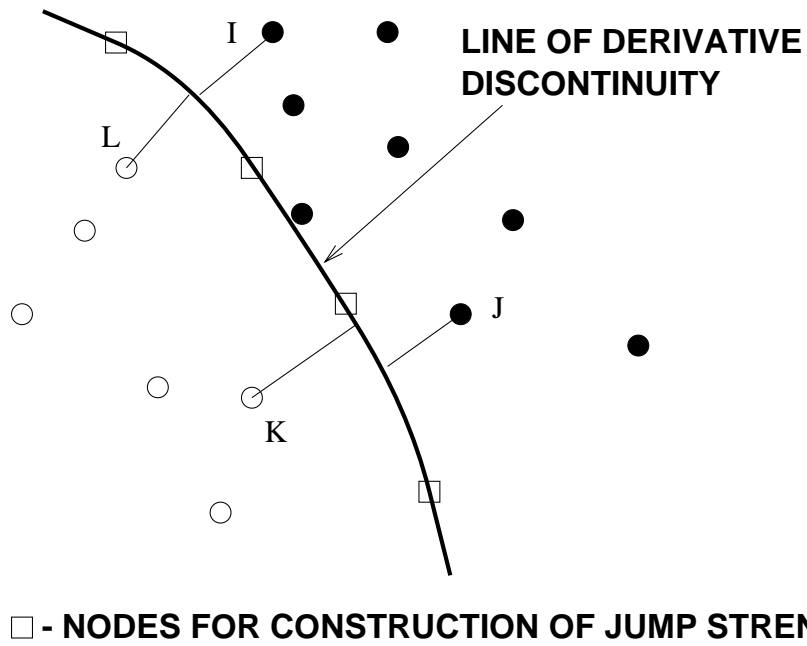
(a)  $\Psi(x)$ (b)  $\Psi_x(x)$ 

Figure 16: Jump term in one dimension



□ - NODES FOR CONSTRUCTION OF JUMP STRENGTH

Figure 17: An example in 2D: For the nodes one one side of the line of discontinuity (filled) the  $r$  is the distance from the node to the line of discontinuity; for the nodes on the other sides of the line (not filled)  $r$  is defined as the negative of the distance from the node to the line of discontinuity. For example,  $r_I$  and  $r_J$  are greater than 0, while  $r_K$  and  $r_L$  are less than 0.

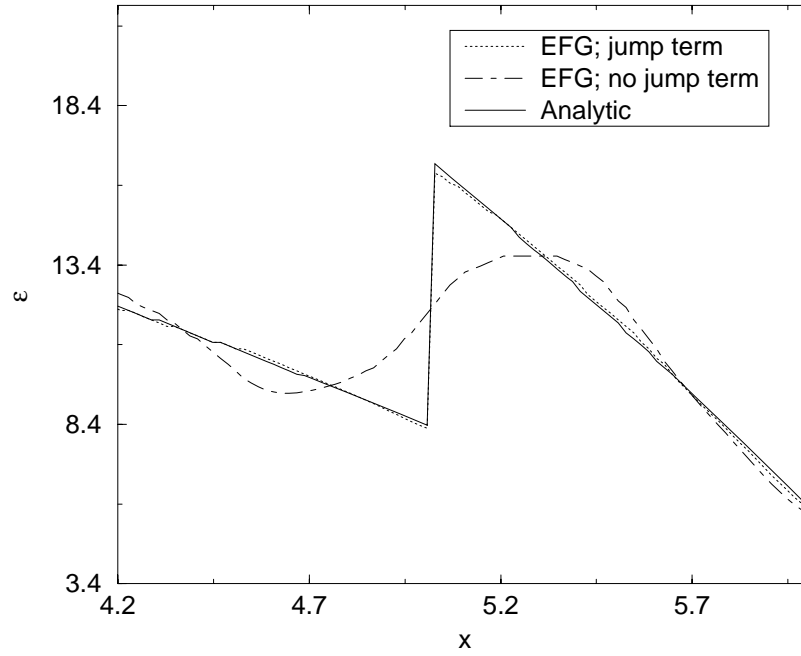


Figure 18: Comparison of the derivative computed with and without the jump term vs. analytic strain for 1D problem. (Magnified view around the discontinuity.)

To illustrate the effectiveness of this addition, we consider a one dimensional and a two dimensional problem. The one dimensional problem is

$$(E(x)u_{,x})_{,x} + x = 0 \quad 0 \leq x \leq 10 \quad (3.10)$$

$$E(x) = \begin{cases} 1 & 0 \leq x < 5 \\ 0.5 & 5 \leq x \leq 10 \end{cases} \quad (3.11)$$

Part of the solution is compared to the analytic solution in Fig 18. Linear MLS approximants were used over 21 nodes using the EFG methodology. As can be seen, in a standard approximation, the discontinuity is smoothed; once the jump term is added, the numerical solution is almost indistinguishable from the exact solution.

For a two dimensional example, we consider the circular inclusion problem described by Cordes and Moran (submitted), in this volume, who treated the interface with Lagrange multipliers. The model is shown in Fig 19 and the strains are shown in 20. While the solution is not as perfect as the one dimensional case, the accuracy is quite good.

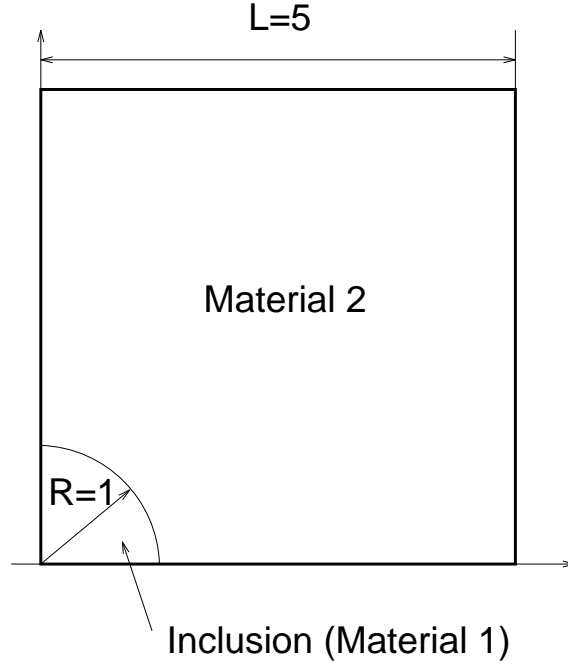


Figure 19: The circular inclusion in the infinite plate problem. (Only the part that is discretized is shown.)

## 4 Numerical Implementation

In the work reported so far, two methods of discretization have been dominant:

1. collocation methods, which are used in SPH,
2. Galerkin methods, which are used in EFG, *hp* clouds, PUFEM, RKPM, and other methods.

### 4.1 Model Equation

In order to discuss the issues associated with discretization, we will consider a general form of the PDE in a domain  $\Omega$  with boundary  $\Gamma$ :

$$\mathcal{L}u(\mathbf{x}) = f(\mathbf{x}) \quad \text{in } \Omega. \quad (4.1a)$$

As a specific equation, we will consider the Poisson equation

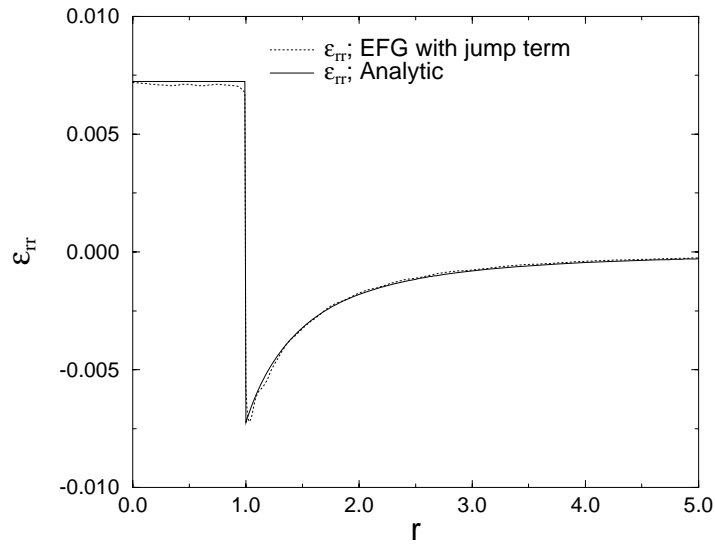
$$\nabla^2 u = f \quad \text{in } \Omega, \quad (4.1b)$$

$$u = \bar{u} \quad \text{on } \Gamma_u, \quad (4.1c)$$

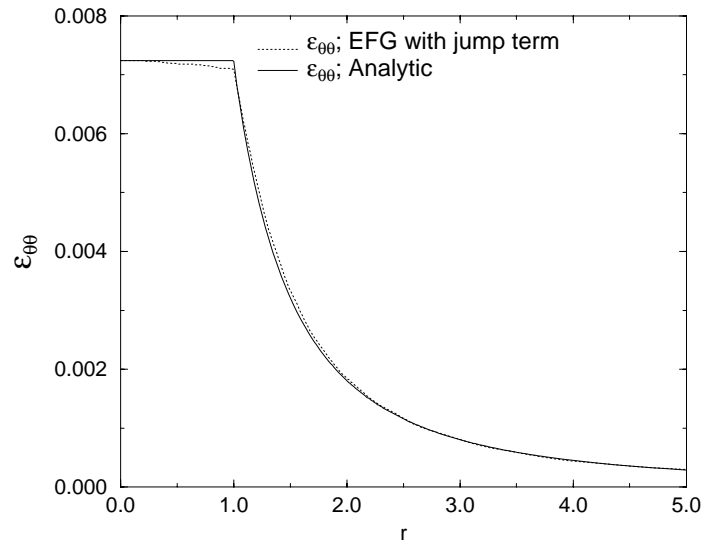
$$u_{,n} = \bar{u}_{,n} \quad \text{on } \Gamma_{un}, \quad (4.1d)$$

where  $\mathbf{n}$  is the direction normal to the boundary.





(a) Radial strain



(b) Hoop strain

Figure 20: A comparison of the radial and hoop strains calculated using EFG with jump term to the analytic solutions.

## 4.2 Collocation Method

Consider a set of  $n_N$  nodes in the domain  $\Omega$ . The approximation is

$$u^h(\mathbf{x}) = \sum_{I=1}^{n_N} \phi_I(\mathbf{x}) u_I. \quad (4.2)$$

Any of the shape functions described previously, e.g. MLS, SPH, or PU, can be used.

In collocation methods, the discrete equations are obtained by enforcing the equation on the set of nodes  $\Omega - \Gamma$  (i.e., the discrete equations are not applied on the boundary nodes). The discrete equations can then be written as

$$\mathcal{L}u^h(\mathbf{x}_J) = f(\mathbf{x}_J) \quad J \in \Omega - \Gamma, \quad (4.3a)$$

$$u(\mathbf{x}_J) = \bar{u}(\mathbf{x}_J) \quad J \in \Gamma_u, \quad (4.3b)$$

$$u_{,n}(\mathbf{x}_J) = \bar{u}_{,n}(\mathbf{x}_J) \quad J \in \Gamma_{un}. \quad (4.3c)$$

The above is a set of  $n_N$  algebraic equations in the unknowns  $u_J$ ,  $J = 1$  to  $n_N$ .

In the particular case of the Poisson equation, the discrete equations are

$$\sum_I \nabla^2 \phi_I(\mathbf{x}_J) u_I = f(\mathbf{x}_J), \quad (4.4a)$$

$$\sum_I \phi_I(\mathbf{x}_J) u_I = \bar{u}_J, \quad (4.4b)$$

$$\sum_I \phi_{I,i}(\mathbf{x}_J) n_i u_I = \bar{u}_{,n}(\mathbf{x}_J). \quad (4.4c)$$

The above procedure is applicable to any of the meshless methods described here which are based on a partition of unity. It should be noted that for the Poisson equation, the interpolants should have  $C^2$  continuity, so in an MLS or SPH approach, the weight function must be  $C^2$ . In the SPH approximation, the discrete equations within the interior take a particularly simple form:

$$\sum_I \nabla^2 w_I(\mathbf{x}_J) u_I \Delta V_I = f(\mathbf{x}_J), \quad (4.5)$$

which in two dimensions can be written as

$$\sum_I \left( \frac{\partial^2 w_I(\mathbf{x}_J)}{\partial x^2} + \frac{\partial^2 w_I(\mathbf{x}_J)}{\partial y^2} \right) \Delta V_I u_I = f(\mathbf{x}_J). \quad (4.6)$$

The above, incidentally, differs somewhat from the discretization as described by Monaghan, where nodal masses are always introduced; this complicates the exposition and is certainly unnecessary in the case of the Poisson equation. If we follow the derivations given in the SPH literature, (4.1b) is multiplied by the weight function

on both sides and integrated over the domain; the left hand side is then integrated by parts twice, giving

$$\begin{aligned} & \int_{\Gamma} w(\mathbf{x} - \bar{\mathbf{x}}) u_{,n}(\bar{\mathbf{x}}) d\Gamma_{\bar{\mathbf{x}}} - \int_{\Gamma} w_{,\bar{n}}(\mathbf{x} - \bar{\mathbf{x}}) u(\bar{\mathbf{x}}) d\Gamma_{\bar{\mathbf{x}}} \\ & + \int_{\Omega} w_{,\bar{n}}(\mathbf{x} - \bar{\mathbf{x}}) u(\bar{\mathbf{x}}) d\Omega_{\bar{\mathbf{x}}} = \int_{\Omega} w(\mathbf{x} - \bar{\mathbf{x}}) f(\bar{\mathbf{x}}) d\Omega_{\bar{\mathbf{x}}} \end{aligned} \quad (4.7)$$

The boundary terms are then dropped, and the integral is discretized, giving

$$\sum_I \left( \frac{\partial^2 w_I(\mathbf{x}_J)}{\partial x^2} + \frac{\partial^2 w_I(\mathbf{x}_J)}{\partial y^2} \right) \Delta V_I u_I = \sum_I w_J(\mathbf{x}_I) f(\mathbf{x}_I) \Delta V_I. \quad (4.8)$$

This is identical to (4.6) except for the RHS, where the weight acts as a filter.

The implementation of these equations is straightforward. At any node  $J$ , one determines the nodes which contain node  $J$  within their domain of influence. In SPH, the construction of the discrete form of the Poisson equations then simply involves calculating the second derivatives of the shape functions of all relevant nodes at node  $J$ , i.e., at  $\mathbf{x} = \mathbf{x}_J$ . The procedure is obviously very fast, though we do not know whether it is stable, and it has only zeroth order consistency. The rates of convergence are later examined for numerical solutions.

For approximations such as moving least square or other partitions of unity, the approximation function and their second derivatives would have to be constructed at each node for all neighbors which interact with it. In the partition of unity of order greater than zero, this involves the solution of the moment equations, which is more time consuming.

### 4.3 Galerkin Method

Discretization by the Galerkin method requires a weak form or variational principle. We will write the weak form as

$$a(\delta u(\mathbf{x}), u(\mathbf{x})) = (\delta u(\mathbf{x}), f), \quad (4.9)$$

where  $\delta u(\mathbf{x})$  is a test function and  $u$  is a trial function. For the specific case of the Poisson equation,

$$a(\delta u, u) = \int_{\Omega} \delta u_{,i} u_{,i} d\Omega, \quad (4.10a)$$

$$(\delta u, f) = - \int_{\Omega} \delta u f d\Omega + \int_{\Gamma_{un}} \delta u \bar{u}_{,n} d\Gamma, \quad (4.10b)$$

where  $\delta u$  vanishes and  $u = \bar{u}$  on  $\Gamma_u$ . Both  $u(\mathbf{x})$  and  $\delta u(\mathbf{x})$  must be at least  $C^0$ .

The implementation of the Galerkin method then is quite similar to the finite element method: select a shape function from Table 1, and use it in (4.9) to obtain the discrete equations:

$$\sum_J \int_{\Omega} \phi_{I,i} \phi_{J,i} d\Omega u_J = f_J, \quad (4.11)$$

where

$$f_J = - \int_{\Gamma_u} \phi_J f d\Omega + \int_{\Gamma_{u_n}} \phi_J \bar{u}_{,n} d\Gamma. \quad (4.12)$$

The major dilemma in meshless methods revolves around how to evaluate the integrals in the above. We have used three approaches:

1. nodal integration, where the integral is evaluated by

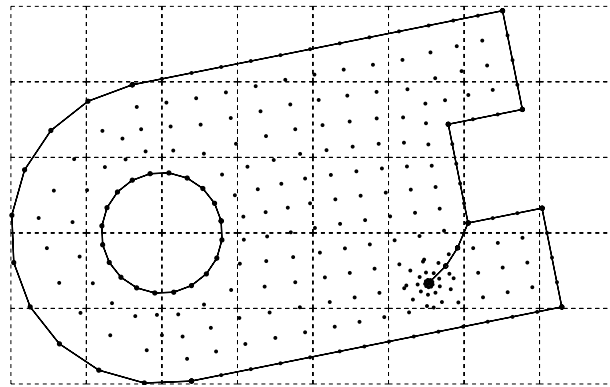
$$\int_{\Omega} f(\mathbf{x}) d\Omega_x = \sum_{I=1}^{n_N} f(\mathbf{x}_I) \Delta V_I \quad (4.13)$$

2. cell or octree quadrature, where a regular array of domains in the background is used for quadrature as shown in Fig. 21a,
3. a background finite element mesh is used for quadrature as shown in Fig. 21b.

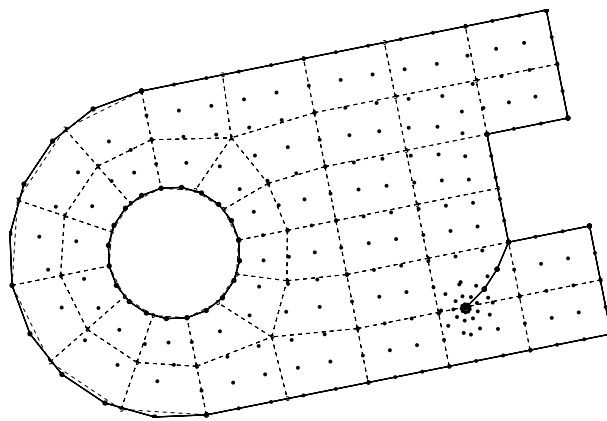
In the second and third cases, either Gauss quadrature or the trapezoidal rule has been used.

The first of these is the fastest, but like nodal collocation appears to suffer from instability. The second and third alternatives have the disadvantage that the resulting method is not truly meshless. Oñate et al. (submitted) have made an appealing definition of meshless methods: those in which the approximation can be constructed strictly in terms of nodes. This definition which permits a background mesh is quite appealing, since a background mesh does not impair the treatment of stationary and moving discontinuities. It should be noted that the background mesh does not need to be compatible with the EFG nodes; thus it can be easily generated from a CAD representation of the model.

The octree background mesh strikes many researchers as unacceptably crude, for within a cell, quadrature is performed over any discontinuities and boundaries which do not coincide with the boundaries of the cells. Our experience so far suggests that the effects are quite minimal. For example, the model in Fig. 22 was used for the near-tip crack problem, where the displacement field corresponding to the asymptotic field near the tip of a mode I crack is prescribed on the boundary. Gauss quadrature was performed using cells whose corners coincided with the nodes. In this case, the line of discontinuity cut through the middle of the cells. The cells which the line of



(a) Cell quadrature



(b) Element quadrature

Figure 21: Quadrature techniques for meshless methods

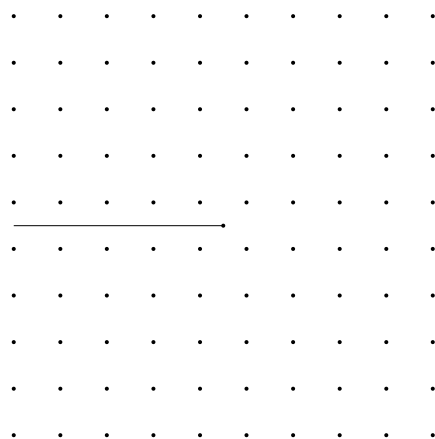


Figure 22: Discrete model for near-tip crack problem.

discontinuity cut were then subdivided so that the cell boundaries were aligned with the discontinuity. No appreciable change in the error in strain energy (1% change) or stress intensity factor (0.1% change) was noticed when the crack was allowed to pass through the middle of the cell.

The shape functions are very complex (see for example Figs. 7 or 12), so a large number of quadrature points must generally be used. We have found it is best to use lower order quadrature in many smaller background cells than to use very high order quadrature in large cells.

Other quadrature schemes have been reported by Yagawa (1995), who constructs a local triangular mesh using mesh generation techniques, and by Nayroles et al. (1992), who use a molecule around the node; they also used a finite element background mesh.

#### 4.4 Essential Boundary Conditions

One of the major difficulties in the implementation of meshless methods is the non-interpolatory character of the approximation, that is, the approximation does not pass through the nodal parameter values. Thus,

$$\phi_I(\mathbf{x}_J) \neq \delta_{IJ} \quad (4.14)$$

As a consequence, the imposition of boundary conditions on the dependent variable, i.e., Dirichlet or essential boundary conditions, is quite awkward. We have worked with several different approaches to this problem:

1. Lagrange multiplier approaches (Belytschko, Lu, and Gu, 1994)

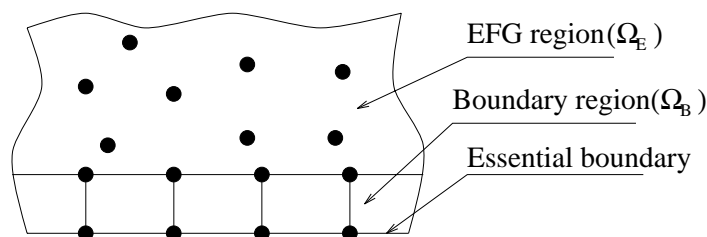


Figure 23: EFG coupled with finite elements along essential boundaries.

2. modified variational principles (Lu, Belytschko, and Gu, 1994)
3. penalty methods
4. perturbed Lagrangian (Chu and Moran, 1995)
5. coupling to finite elements (Krongauz and Belytschko, to appear)

The disadvantage of the first approach is that the discrete equations for a linear self-adjoint PDE are no longer positive definite nor banded. However, the Lagrange multiplier method is the most accurate method for imposing Dirichlet boundary conditions and, therefore, is quite useful for smaller problems, such as smaller two-dimensional problems, where the cost of solving the equations is immaterial. The approach based on the modified variation principle results in banded equations, but the boundary conditions are not imposed with as high a degree of accuracy.

For practical purposes, the coupled FE-EFG approach appears to be most satisfactory. In this approach, elements are placed around the boundary of the domain as shown in Fig. 23 and the meshless approximation is coupled to the finite element approximation as described later; essential boundary conditions are applied to finite element nodes by standard methods. This approach is particularly useful when finite elements are used as a background mesh for quadrature, since then a finite element mesh is already available. Note however, that only the elements adjacent to the boundary are used for purposes of approximation.

Another approach to imposing boundary conditions has been developed by Gosz (1996) who imposes the condition by forcing the weight function to go to zero on Dirichlet boundaries. This approach is very appealing, but may be less robust than other techniques.

## 4.5 Coupling to Finite Elements

It is advantageous to couple meshless methods with finite element methods. Meshless methods, particularly in the current state of development, are still not as fast as finite element methods. Therefore, it is desirable to use meshless models only in those subdomains where their greater versatility is needed. For example, in problems of crack

propagations, sub-domains where cracks are anticipated can often be determined *a priori*. It is then useful to use the meshless methods only in those sub-domains and a finite element model for the rest. In the future, it may become possible to automatically shift between finite element and meshless approximation according to the needs of a solution.

Several methods for coupling with finite elements have been developed. One of the first was by Johnson (1994) and Attaway et al. (1994), who coupled SPH to finite elements. The results presented are quite good, but no demonstration of the consistency of the coupling was given; this is not surprising since SPH by itself is not consistent. As noted before, the lack of linear consistency does not necessarily imply that the method is not convergent.

A technique for coupling MLS-based meshless method was presented by (Hegen, 1994). Hegen took advantage of the fact that the MLS formulation becomes a finite element approximation when the domain of influence coincides with the element. Therefore, by setting the domains of influence in the meshless domain adjacent to the finite element domain to coincide with virtual elements, he was able to develop a consistent coupling.

An alternative form of coupling EFG to finite elements has been developed by Belytschko, Organ, and Krongauz (1995). This coupling is based on a blending approach where blending functions are used to combine the finite element and meshless approximations on the interface zone. The form of the blending is as follows:

$$u = R_s u^{EFG}(\mathbf{x}) + (1 - R_s) u^{FE}(\mathbf{x}), \quad (4.15)$$

where

$$R_s = f(R), \quad R = \sum_{I: \mathbf{x}_I \in \Gamma_{EFG}} N_I^{FE}(\mathbf{x}). \quad (4.16)$$

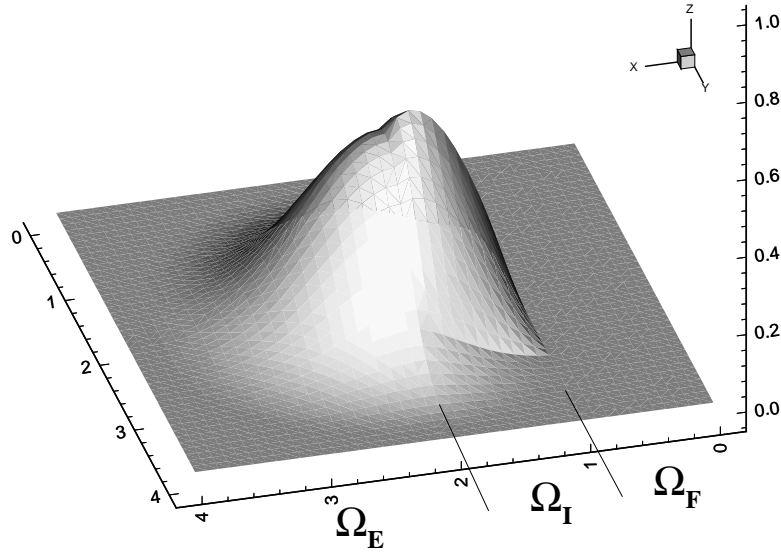
This method satisfies consistency and is quite robust. The only disadvantage we have noticed is the resulting complexity of the shape functions in the interface domain; see Fig. 24. This, of course, entails higher order quadrature. We are still working on techniques with the aim of obtaining consistent couplings with less baroque shape functions.

A procedure with a similar outcome which is theoretically quite appealing was developed by Liu, Chen, and Uras (1995) and Liu, Chen, Chang, and Belytschko (1996). The approach, rather than explicitly invoking a blending function, combines finite element and meshless approximations in the interface domain by enforcing that the approximation be consistent. The resulting shape functions are almost identical to those obtained by the blending approach.

## 4.6 Improvements in Function and Derivative Computation

From a first glance at MLS and PU type meshless methods, their major disadvantage appears to be the additional computational time associated with the construction of





(a) Shape function.

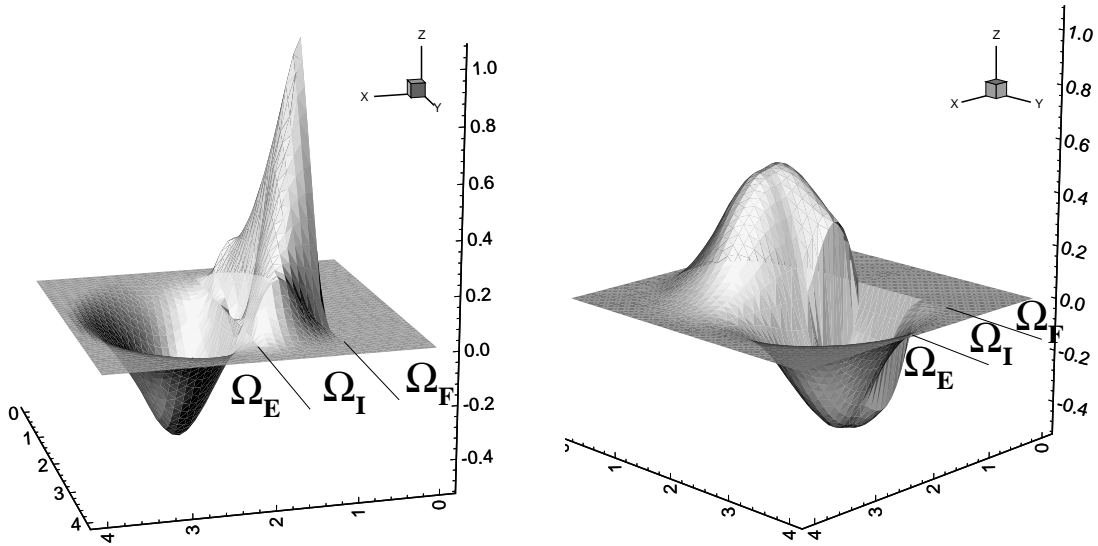
(b) Shape function  $x$ -derivative.(c) Shape function  $y$ -derivative.

Figure 24: Two dimensional FE-EFG coupled shape function and derivatives for a node on the EFG boundary of an interface element.

shape functions and their derivatives. The three most time intensive parts of shape function computation described in Section 2.2 are:

1. computation of moments;
2. matrix inversion;
3. matrix-matrix and matrix-vector multiplies.

The derivative calculations are even more computationally intensive than the shape function construction. Even for a linear basis this burden exceeds the cost of the inversion of the Jacobian required in the isoparametric finite element method. By contrast, SPH requires far fewer computations than MLS or PU methods but it is not consistent or stable.

In this section, we develop two techniques which can provide substantial improvement in computational cost:

1. A derivative calculation, based on consistency which appeared in Belytschko, Krongauz, Fleming, Organ, and Liu (to appear).
2. A consistency technique in Krongauz and Belytschko (submitted,a) based on combining derivatives in different directions.

**Derivatives based on consistency** The linear consistency requirements for shape functions  $\phi_I(\mathbf{x})$  are

$$\sum_I \phi_I(\mathbf{x}) = 1, \quad (4.17a)$$

$$\sum_I \phi_I(\mathbf{x}) x_I = x, \quad (4.17b)$$

$$\sum_I \phi_I(\mathbf{x}) y_I = y. \quad (4.17c)$$

Then, repeating some of the equations in Section 2.2,

$$\phi_I(\mathbf{x}) = \boldsymbol{\alpha}^T \mathbf{p}(\mathbf{x}) \mathbf{w}_I(\mathbf{x}), \quad (4.18)$$

$$\mathbf{A} \boldsymbol{\alpha} = \mathbf{p}(\mathbf{x}) = \begin{bmatrix} 1 \\ x \\ y \end{bmatrix}. \quad (4.19)$$

It is computationally convenient to shift the origin of coordinates to the point of evaluation  $(x', y')$  with (4.19) becoming

$$\overline{\mathbf{A}} \overline{\boldsymbol{\alpha}} = \begin{bmatrix} 1 \\ 0 \\ 0 \end{bmatrix}, \quad (4.20)$$

with

$$\bar{A}_{ij} = \sum_K w_K(\mathbf{x}) p_i(\mathbf{x}_K - \mathbf{x}') p_j(\mathbf{x}_K - \mathbf{x}'). \quad (4.21)$$

Let us differentiate (4.19) with respect to  $x$ . (We will compute everything in the shifted coordinate system as in (4.21) and so will not use the bar notation to differentiate quantities computed in the original and shifted coordinate systems.) Then

$$\mathbf{A}_{,x} \boldsymbol{\alpha} + \mathbf{A} \boldsymbol{\alpha}_{,x} = \mathbf{p}_{,x}(\mathbf{x}) = \begin{bmatrix} 0 \\ 1 \\ 0 \end{bmatrix}. \quad (4.22)$$

First, to solve (4.19) for  $\boldsymbol{\alpha}$ ,  $\mathbf{A}$  is LU decomposed, with the decomposition stored. Then since we already know  $\boldsymbol{\alpha}$  we can solve

$$\mathbf{A} \boldsymbol{\alpha}_{,x} = \mathbf{p}_{,x} - \mathbf{A}_{,x} \boldsymbol{\alpha} \quad (4.23)$$

for  $\boldsymbol{\alpha}_{,x}$ . Because we already have the LU decomposition of  $\mathbf{A}$  we just need to perform a back substitution plus one matrix-vector product to get  $\boldsymbol{\alpha}_{,x}$ . Similarly,

$$\mathbf{A} \boldsymbol{\alpha}_{,y} = \mathbf{p}_{,y} - \mathbf{A}_{,y} \boldsymbol{\alpha}, \quad (4.24)$$

with

$$\mathbf{p}_{,y}(\mathbf{x}) = \begin{bmatrix} 0 \\ 0 \\ 1 \end{bmatrix}. \quad (4.25)$$

The derivatives of the shape functions are then given by

$$\begin{aligned} \phi_{I,j} &= (\alpha_1 + \alpha_2(x_I - x') + \alpha_3(y_I - y')) w_{I,j} \\ &\quad + (\alpha_{1,j} + \alpha_{2,j}(x_I - x') + \alpha_{3,j}(y_I - y')) w_I. \end{aligned} \quad (4.26)$$

Higher derivatives can be obtained by the same technique, i.e., by differentiating (4.22) and (4.24) and shifting all the known terms to the right side of the equation and using previously obtained LU decomposition to do back substitution.

The above technique for computing shape functions and their derivatives is about twice as fast as standard EFG when used in two dimensions with  $s_{max}$  equal to 2.

**Consistency based on linear combination of derivatives** A second approach to speeding up the calculations is based on combining the derivatives of the weight functions so that first order consistency is satisfied (Krongauz and Belytschko, submitted,a). The consistency condition is applied directly to the derivatives.

We consider the process in two dimensions. The objective is to find shape functions  $\phi_I$  such that they satisfy the linear consistency conditions in two dimensions. If we

differentiate (4.17) we obtain consistency conditions on the derivatives of the shape functions:

$$\sum_I \phi_{I,x}(\mathbf{x}) x_I = 1, \quad (4.27a)$$

$$\sum_I \phi_{I,y}(\mathbf{x}) x_I = 0, \quad (4.27b)$$

$$\sum_I \phi_{I,x}(\mathbf{x}) y_I = 0, \quad (4.27c)$$

$$\sum_I \phi_{I,y}(\mathbf{x}) y_I = 1. \quad (4.27d)$$

The consistency conditions (4.27) are satisfied using the following procedure. The shape functions are replaced by

$$\tilde{\phi}_{I,x} = \alpha_1 \phi_{I,x}^0 + \alpha_2 \phi_{I,y}^0, \quad (4.28a)$$

$$\tilde{\phi}_{I,y} = \beta_1 \phi_{I,x}^0 + \beta_2 \phi_{I,y}^0. \quad (4.28b)$$

Since the  $\phi_I^0$ 's represent partitions of unity (see Eq. (2.27)), the constant consistency conditions

$$\sum_I \tilde{\phi}_{I,x} = 0, \quad (4.29a)$$

$$\sum_I \tilde{\phi}_{I,y} = 0, \quad (4.29b)$$

are always satisfied no matter what  $\boldsymbol{\alpha}$  and  $\boldsymbol{\beta}$  are. Substituting (4.28) into (4.27) we obtain the following systems of equations:

$$\mathbf{A}\boldsymbol{\alpha} = \mathbf{r}_1, \quad (4.30a)$$

$$\mathbf{A}\boldsymbol{\beta} = \mathbf{r}_2, \quad (4.30b)$$

where

$$\mathbf{A} = \begin{bmatrix} \sum_I \phi_{I,x}^0 x_I & \sum_I \phi_{I,y}^0 x_I \\ \sum_I \phi_{I,x}^0 y_I & \sum_I \phi_{I,y}^0 y_I \end{bmatrix}, \quad (4.31)$$

$$\mathbf{r}_1 = \begin{bmatrix} 1 \\ 0 \end{bmatrix} \quad \mathbf{r}_2 = \begin{bmatrix} 0 \\ 1 \end{bmatrix}. \quad (4.32)$$

By solving the system of equations for two right hand sides simultaneously (e.g., LU decomposition of  $\mathbf{A}$ ), we obtain the shape function derivatives that satisfy the constant (4.29) and linear (4.27) consistency conditions.

The “derivatives” have a shortcoming, however. In general, there does not exist a function  $\phi_I$  such that its  $x$  and  $y$  derivatives are  $\phi_{I,x}$  and  $\phi_{I,y}$ . So  $\phi_{I,x}$  and  $\phi_{I,y}$  should really be thought of as 2 separate sets of functions which interpolate the  $x$  derivative and the  $y$  derivative, respectively. In other words, the derivatives are not compatible.

The fact that the shape functions themselves are not available is not important in partial differential equations where the function itself does not appear. For the case where it does appear, a modified Petrov-Galerkin procedure described in Krongauz and Belytschko (submitted,a) could be used. The only places in the Galerkin statement of the elasticity problem which require interpolation of the function itself are the body force term and the traction term.

## 4.7 Cost of EFG Computations

One of the major factors influencing the success of a methodology is the cost vs. accuracy dependence. The EFG method is meshless, which means that there are selectable parameters (e.g., the sizes of the domains of influence) affecting both the cost and the accuracy. How to make the optimal choice is at present unclear. The cost of the computation for implicit EFG methods is strongly affected by the number of nodes  $n_n$  involved at an integration point ( $n_n$  depends on the size of the domain of influence). In fact, the cost to assemble the stiffness matrix is proportional to  $n_n^2$ . The accuracy is not a simple function of  $s_{max}$ , which makes it difficult to optimize the needed choices.

The cost vs. accuracy relationship was explored for 3D elastostatics. Numerical solutions were obtained for the classical Kelvin problem of stress distribution in an infinite elastic medium loaded by a concentrated force. The displacements and the stresses are singular at the applied force. The simulation was run for a cube cut out of the infinite medium close to the applied force (note that the load was applied *outside* the cube), with the exact displacements prescribed at the farthest face from the load, and the exact tractions prescribed at all the other faces.

The EFG model consisted of  $N \times N \times N$  integration cells, with the EFG nodes located at the vertices of the cells. The essential boundary conditions were enforced on the face where the displacements were prescribed by the FE-EFG coupling methodology (this amounts to a modification of the EFG shape functions to be identical with FE shape functions on the boundary of the EFG domain).

The parameters varied in the simulation were (i) the domain of influence radius  $d_m$ , and (ii) the quadrature order ( $n_g \times n_g \times n_g$  Gaussian quadrature was performed). The monitored quantity was the approximate strain energy normalized by the exact strain energy. The computations were run for EFG grids with  $N = 4$  and  $N = 8$  and  $d_m = 1, 1.25, 1.5$ , and for FE grids composed of usual linear hexahedral elements with  $N = 4, 8, 12, 16$ .

The results were summarized in Fig. 25. It can be seen that when cost for an EFG computation is compared to an FE solution with the same number of unknowns, the

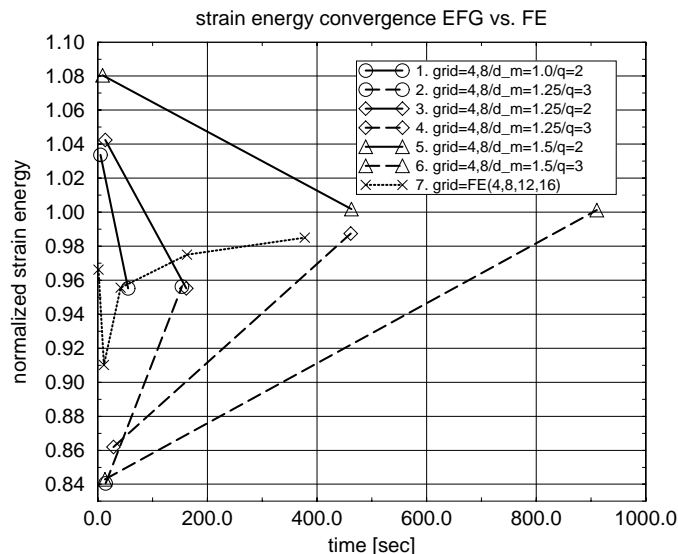


Figure 25: Comparison of cost vs. accuracy of the strain energy for the Kelvin problem

FE results are much less expensive. However, comparing the costs based on the approximation accuracy, the results can be quite different. In this study, it can be seen that the desired accuracy (2% error in strain energy) can be obtained for approximately the same cost by both FE and EFG—compare curves 4, 5, and 7 in Fig. 25. Note that the results obtained in this case by the EFG method have the advantage of providing better (smooth) approximation of stresses.

## 5 Plates, Shells, and Nonlocal Materials

MLS approximations are very attractive for plates and shells because of the ease with which  $C^1$  continuity can be achieved. Applications to plates were first investigated by Hein (1993), who did not achieve much success for various reasons: use of point collocation to enforce essential boundary conditions, too small supports, unsuitable weight functions, etc.

Lu, Gu, and Belytschko (1996) treated Mindlin-Reissner plates with linear and quadratic basis EFG. Results were poor due to shear locking. Krysl and Belytschko have treated plates and shells with  $C^1$  approximations. The EFG method has been applied in Krysl and Belytschko (1996a) to thin (Kirchhoff) plates. Background quadrilateral elements were used for the purpose of Gaussian numerical integration. The EFG nodes were generated at the vertices of the geometric subdivision. Numerical experiments to determine the optimal quadrature order indicated that  $6 \times 6$

quadrature was close to optimal with respect to cost and accuracy. The complete quadratic polynomial basis was used. Therefore, consistency was achieved automatically. The  $C^1$  quartic spline weight function with a circular domain of influence was adopted. Thus, smooth moments could be obtained without any re-interpolation or smoothing. The essential boundary conditions were enforced by Lagrange multipliers. The high accuracy and versatility of the present numerical approach were demonstrated on a number of examples: a square plate under a concentrated load (clamped and simply-supported), and a circular clamped plate for both uniform and irregular (but not graded) grids. An attempt to optimize the accuracy of the method by the choice of the weight function support size was undertaken. A numerical study indicated that a support radius of approximately 3.9 node spacings yielded the best results for all the problems studied for regular as well as irregular grids.

The EFG method has also been applied to thin (Kirchhoff-Love) shells in Krysl and Belytschko (1996b). Background elements (quadrilaterals) were used for the purposes of surface shape approximation and numerical integration. The EFG nodes were generated at the vertices of the geometric subdivision. The shape of the surface was approximated by the moving least squares technique from the vertices of the background mesh. An algorithm for the automatic parameterization of the background mesh was proposed. Numerical integration was carried out on the background elements by a  $6 \times 6$  Gaussian quadrature. The complete quadratic and quartic polynomial basis was used, so consistency was achieved automatically. The weight function was the quartic spline as in the previous work on plates. The essential boundary conditions were enforced by Lagrange multipliers. The obstacle course for shells from Belytschko et al. (1985) was solved for a quadratic polynomial basis. The membrane locking which appeared was alleviated by enlarging the domains of influence of the EFG nodes for the quadratic basis, and was removed completely by using the quartic basis.

Methods to remove locking in low order approximations are more difficult to devise for the MLS schemes than for finite elements because of the diffuse character of the approximation. For example, it precludes successful reduced integration.

Chu and Moran (1995) have applied EFG to problems with nonlocal materials of a gradient type. In these materials, the stress depends on a gradient of the strains, so  $C^1$  continuity is required in the approximation. While this is difficult to achieve in finite elements, they were easily able to achieve such continuity with MLS approximations. Results were obtained for a variety of phase transformation problems.

## 6 Convergence

Duarte and Oden (1996) have shown that the rate of convergence for the  $hp$ -clouds approximations is given by

$$|u(\mathbf{x}) - u^h(\mathbf{x})|_{m,\Omega} \leq Ch^{k+1-m} |u|_{k+1,\Omega} \quad (6.1)$$

where  $h$  is the window size,  $k$  is the polynomial degree of the basis,  $m$  is the order of the governing equation, and the (semi)norms are the usual  $L_2$ -generated norms on Sobolev spaces. Liu, Li, and Belytschko (1996) have obtained similar results for the more restrictive case of a kernel (or MLS) approximation. In all cases the results have been restricted to convex domains with Lipschitz continuous boundaries.

When the EFG shape functions are constructed on nonconvex domains (e.g., in domains containing cracks) by invoking the visibility criterion, the resulting approximation is not  $C^0$ —the shape functions have discontinuities along radial directions emanating from the non-convex boundaries. Krysl and Belytschko (to appear) have shown that the discontinuous EFG approximations are convergent by invoking well-known results from the theory of non-conforming finite elements. The non-conforming EFG method was first studied by the approach proposed by Stummel (1979), i.e., by the generalized patch test and the classical patch test of Strang and Fix (1973). Both tests showed that the so-called consistency error tends to zero as the grid is refined, and the convergence of the non-conforming EFG was thus established. The convergence rate of the EFG method was established by inspecting the approximation error. The approach of Ciarlet (1991) was adopted, and the approximation error was estimated for the conforming variant by using the properties of a polynomial-preserving operator. The effect of reentrant corners (and other non-smooth boundaries) on the convergence rate was then obtained for the conforming variant following the well-established estimate based on fractional Sobolev spaces pioneered by Babuška and others.

The consistency error was estimated for the non-conforming EFG variant by a direct inspection of the consistency term. The following results were obtained for the convergence rates ( $k$  is the polynomial degree of the basis):

1. For models properly graded to account for the singularity, the consistency term due to the non-conformity of the EFG basis governs the rate of convergence for  $k > 1$ . Thus, only the conforming variant of the EFG method should be used with higher-order bases.
2. For a linear basis ( $k = 1$ ), the rate of convergence is not affected by the discontinuous shape functions. For a quasi-uniform mesh, the error is governed by the singularity due to the nonconvex boundaries, and for properly graded meshes both the approximation ability and the consistency term estimate the same rate of convergence, equal to one.

An extension of these results to three-dimensional, polyhedral domains, is not trivial, since, in addition to vertex (conical) singularities, edge singularities need to be considered (possibly along curved edges).



## 7 Results

### 7.1 Convergence Studies

**One dimensional Poisson equation** The following equation is considered:

$$u_{,xx}(x) - 2 = 0 \quad 0 < x < 8, \quad (7.1)$$

with boundary conditions

$$u(0) = 0, \quad (7.2a)$$

$$u(8) = 64. \quad (7.2b)$$

The exact solution is given by

$$u(x) = x^2. \quad (7.3)$$

Equispaced nodal arrangements of 9, 17, 33, 65, 129, and 257 nodes were used to test convergence of EFG with MLS approximations with different supports,  $s_{max}$ . The value of  $s_{max}$  was computed by  $s_{max} = s_m h$  where  $h$  is the nodal spacing. Four point Gaussian quadrature was used in cells between nodal pairs. The convergence of displacements is shown in Fig. 26 and convergence of derivatives in Fig. 27. It can be observed that for  $s_m = 1.1$  the convergence results are almost identical to the linear finite element results.

Convergence rates in both energy and displacement norms increase when  $s_m$  increases from 1.1. However, we do not observe *any* exponential convergence, and we have observed exponential convergence only when  $s_{max}$  is not proportional to  $h$ .

**Two dimensional Poisson equation** We consider the convergence of several of the methods discussed so far using the Poisson equation

$$\nabla^2 u = 4 \quad 0 < x < 2 \quad 0 < y < 2 \quad (7.4)$$

with boundary conditions

$$u = x^2 + y^2 \text{ on } \Gamma_u \quad (7.5)$$

with  $\Gamma_u = \Gamma$ .

Equispaced meshes of  $3 \times 3$ ,  $5 \times 5$ ,  $7 \times 7$ , and  $21 \times 21$  nodes were used with  $4 \times 4$  Gaussian quadrature in each cell. EFG with  $k = 1$  (linear basis), DEM (Nayroles, Touzot, and Villon, 1992) and Shepard approximations were used in the study; DEM is distinguished from EFG by the absence of the derivatives  $\mathbf{a}_{,i}$ . The convergence results in  $L_2$  norm are shown in Fig. 28 and in  $H_1$  norm in Fig. 29. It can be observed that DEM's and Shepard interpolant's performance decreases as  $s_{max}$  is increased, while EFG performs better.

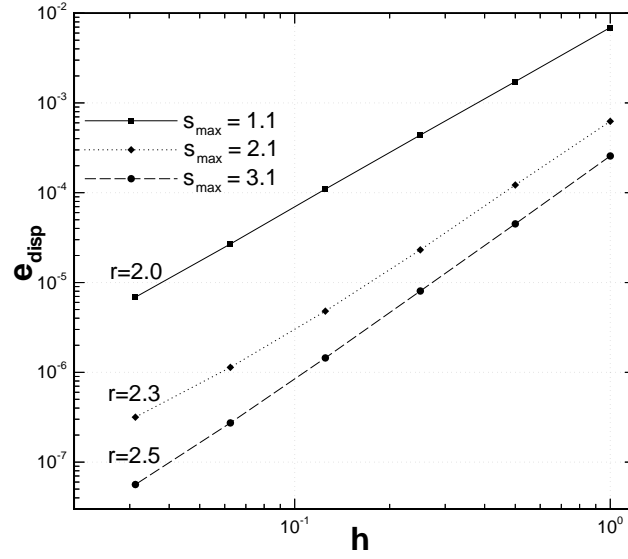


Figure 26: Convergence of displacements in one dimension. The rates are indicated by the value of  $r$ . The results are normalized by the norm of the exact solution.

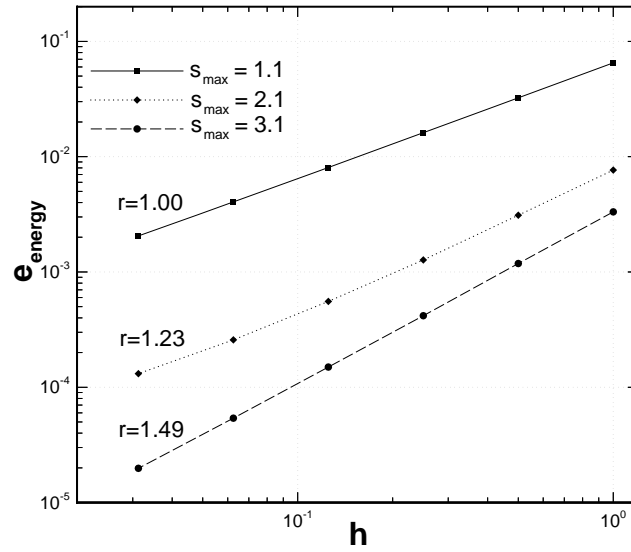


Figure 27: Convergence in energy norm in one dimension. The rates are indicated by the value of  $r$ . The results are normalized by the energy norm of the exact solution.

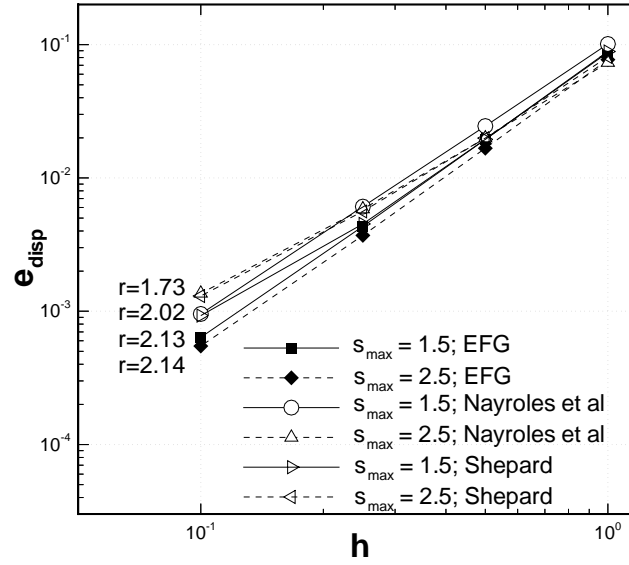


Figure 28: Convergence in  $L_2$  norm of  $u(\mathbf{x})$  for the Poisson equation in two dimensions. Convergence rates are indicated by the value of  $r$ .

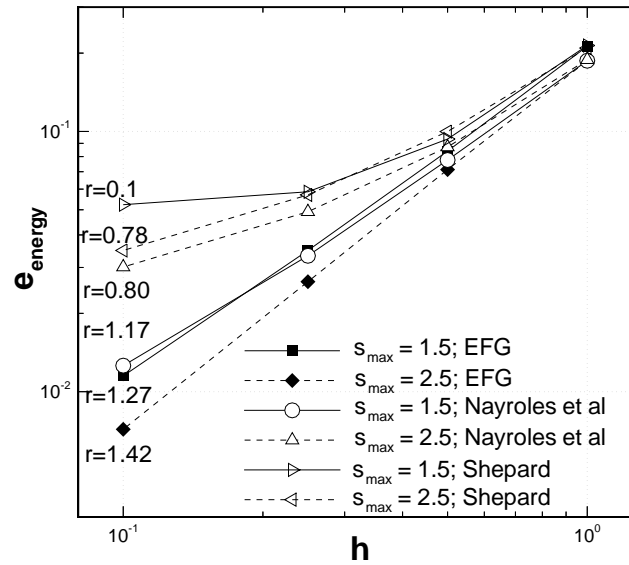


Figure 29: Convergence in  $H^1$  norm of  $u(\mathbf{x})$  for the Poisson equation in two dimensions. Convergence rates are indicated by the value of  $r$ .

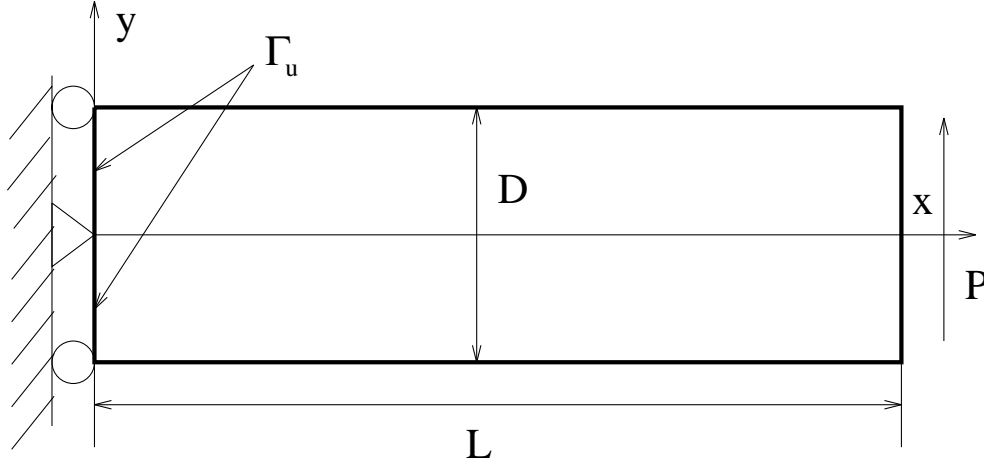


Figure 30: Cantilever Beam

## 7.2 Cantilever Beam

Consider a cantilever beam subject to end load as shown in Fig. 30. The objective of this problem is to examine whether SPH approximations converge by using such a set of weight functions and nodal volumes as to make SPH shape functions identical to Shepard interpolants. The question of whether SPH approximations with collocation are convergent is difficult to resolve, since that combination is not stable, so the discrete equations are singular. Our approach here is to use Shepard approximations with a Galerkin discretization and a background mesh for quadrature; we assume that the approximation behavior is not adversely affected by more sampling. At the same time, we examine the convergence of the DEM approximation of Nayroles et al. (1992), which drops  $\mathbf{a}_{,i}$ .

The solution is given by Timoshenko and Goodier (1970) as

$$u_x = \frac{-Py}{6EI} \left[ (6L - 3x)x + (2 + \nu)(y^2 - \frac{D^2}{4}) \right] \quad (7.6)$$

$$u_y = \frac{P}{6EI} \left[ 3\nu y^2(L - x) + (4 + 5\nu)\frac{D^2 x}{4} + (3L - x)x^2 \right] \quad (7.7)$$

The stresses are given by

$$\sigma_{xx} = \frac{P(L - x)y}{I} \quad (7.8)$$

$$\sigma_{yy} = 0 \quad (7.9)$$

$$\sigma_{xy} = \frac{P}{2I} \left( \frac{D^2}{4} - y^2 \right) \quad (7.10)$$

where  $I$  is the moment of inertia and for a beam with rectangular cross-section and

unit thickness it is given by

$$I = \frac{D^3}{12} \quad (7.11)$$

The displacements (7.6) and (7.7) are prescribed as essential boundary conditions at  $x = 0$ ,  $-D/2 \leq y \leq D/2$ ; the remaining boundaries are traction boundaries.

The following parameters were used for the cantilever beam problem:  $E = 1000$ ;  $\nu = 0.3$ ;  $D = 1$ ;  $L = 8$ . Regular meshes were used, with 3x3 Gaussian quadrature in each cell. Four node isoparametric elements were used to construct the modified shape functions along the boundary. The support of the weight function  $s_{max}$  was computed as follows:

$$s_{max}^I = s_m \max(\Delta x, \Delta y) \quad (7.12)$$

Errors in energy convergence plots are shown in Fig. 31, and the rate of convergence is indicated by the value of  $r$ . Shepard interpolants give very poor results for this problem: no convergence was observed for the meshes used. A possible explanation is that in this problem the ratio of regions near the boundary to the interior regions is high. Since Shepard approximations are poor near the boundaries (i.e., the deviation from linear consistency is greatest there), this may explain the poor performance. As evidence supporting this explanation it should be said that when a “beam” problem with dimension 8 by 8 was analyzed, Shepard interpolants performed much better.

### 7.3 Elastostatic Fracture

The objective of the remainder of this section is to present some of the capabilities of meshless methods which have been developed so far in this group. Problems dealing with crack propagation, both static and dynamic, are considered. Results for a three-dimensional Taylor bar problem are also reported. The problems were all solved by the element-free Galerkin method (EFG) with linear MLS approximations. Background finite elements were used for quadrature.

**Double Cantilever Beam** This example concerns the propagation of a fatigue crack in a double cantilever beam (DCB) specimen. The geometry is shown in Fig. 32, with  $L = 300$  mm,  $h = 100$  mm,  $a = 138$  mm, and  $P = 100$  N. The model is elastostatic and the Paris law was used for crack evolution. Plane stress linear elastic conditions are assumed with Young’s modulus  $E = 200$  GPa and Poisson’s ratio  $\nu = 0.3$ . All calculations were performed using a linear basis and a star-shaped array of nodes was placed at the crack tip for enhanced spatial resolution. A small perturbation at an angle  $d\theta = 4.8^\circ$  with  $\Delta x = 12$  mm is introduced at the crack tip to trigger the crack path instability. The progression of fatigue crack growth is shown in Figs. 33. Note that the crack passes quite arbitrarily through the array of

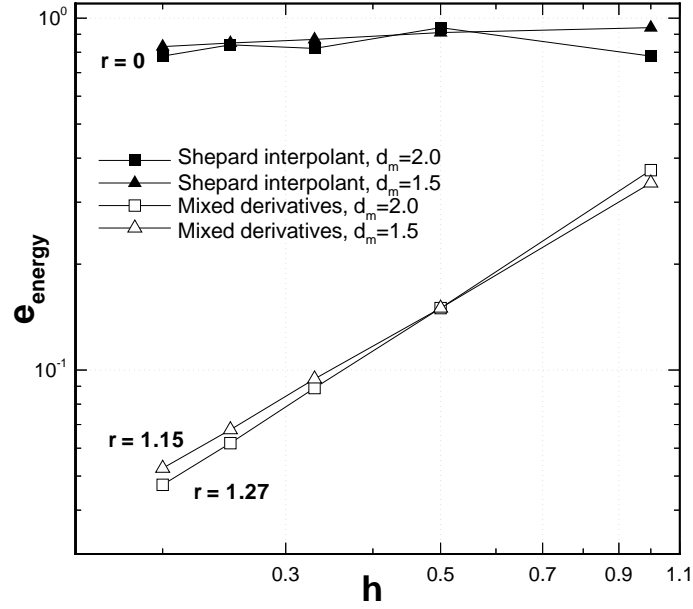


Figure 31: Strain energy convergence plot for the cantilever beam problem; convergence rates are indicated by the value of  $r$ .

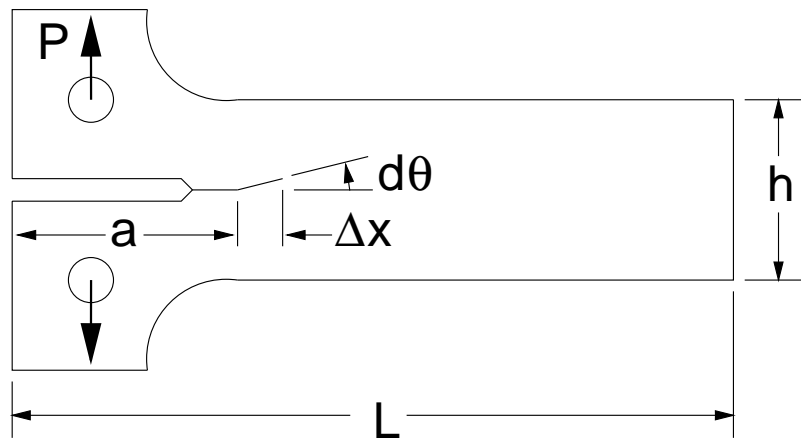


Figure 32: Double cantilever beam (DCB) specimen geometry.

nodes. Experimental results for this problem are presented in Sumi, Nemat-Nasser, and Keer (1985) and Sumi (1985), who also reports finite elements studies.

**Crack growth from a fillet** The next example shows the propagation of a fatigue crack from fillet. The setup is shown in Fig. 34, with the actual domain modeled outlined with a dashed line. Sumi, Yang, and Wang (submitted) performed experiments on a similar structure, but in addition to the loading, they included the influence from welding residual stresses and varied the size of the bottom I-beam to alter the bending stiffness of the beam. These calculations do not include the effects of the welding residual stresses, and the effect of the bottom I-beam is simplified. The only cases reported are the very thick I-beam (rigid boundary) and very thin I-beam (free boundary). The material properties are the same as in the previous example, and the applied load is  $P = 1.0$  N. A linear basis was used and a star-shaped array of nodes was placed at the crack tip for added spatial resolution. The fillet radius is  $\rho = 10$  mm.

The progression of fatigue crack propagation is shown in Figs. 35 for the case of the very thin I-beam. The calculations were completely automatic with no remeshing or restarts.

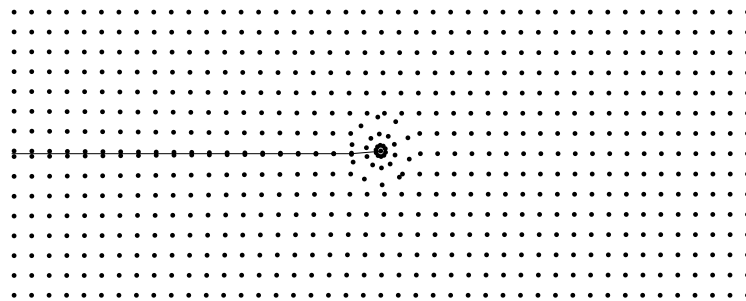
## 7.4 Elastodynamic Fracture

**Edge-Cracked Plate under Impact Loading** The first dynamic fracture example is an experiment from Kalthoff and Winkler (1987). In these experiments, a free plate of high strength maraging steel with two edge notches was loaded between the notches by a projectile; see Fig. 37. (Kalthoff at the 1995 winter ASME meeting reported these experiments were actually with a single notch specimen.) At lower strain rates, failure occurred in a brittle fracture mode, where the crack propagated at an angle of about  $70^\circ$  with respect to the original notch.

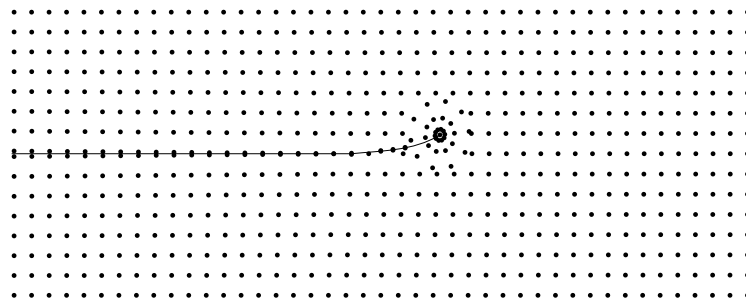
We model the tensile fracture mode using EFG coupled to finite elements (Belytschko, Organ, and Krongauz, 1995). Taking advantage of symmetry, only the top half of the plate was modeled; a small initial crack was placed at the tip at a  $70^\circ$  angle. Details of this analysis are given in Organ (1996). The crack path from the numerical solution is shown in Fig. 38; the angle of the numerical path is slightly larger than the experimental result, around  $77^\circ$ . Results for EFG using a model with a sharp notch have been reported by Belytschko and Tabbara (1996).

**Crack Propagation in Concrete** John and Shah (1990) have reported results from fracture tests on concrete 3-point-bend specimens subjected to impact loading using a Charpy system. Each specimen was pre-notched at an offset from the midspan; the specimen geometry is shown in Fig. 39. The notch location was described in terms of a normalized parameter,  $\gamma = a/2$ .

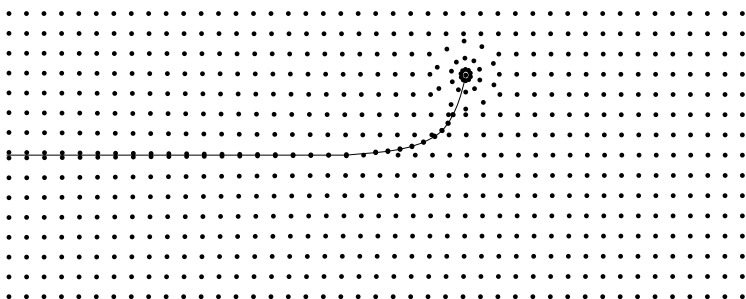
John (1988) reports crack paths for specimens with the offset notch at various



(a)



(b)



(c)

Figure 33: Crack path progression in DCB specimen with an initial perturbation  $d\theta = 4.8^\circ$ .



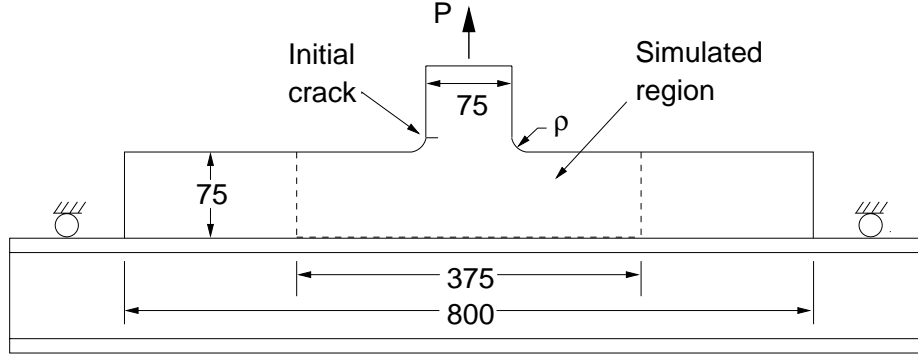


Figure 34: Experimental geometry from Sumi, et al.

locations, and observed a *transition point*,  $\gamma_t$ , at which the beam could fail either at the midspan or the offset notch. For  $\gamma > \gamma_t$ , the specimen would fail at the midspan, and for  $\gamma < \gamma_t$ , failure would occur at the notch;  $\gamma_t = 0.77$ .

Although concrete fracture is well known *not* to be predictable without a process zone, we use elastodynamic fracture mechanics to illustrate the performance of EFG with complicated crack paths and see whether elastodynamics has some predictive value here. The discretization consists of  $72 \times 24$  cells with nodes placed at the corners of each cell. To model the failure transition point  $\gamma_t$ , an additional crack was introduced at the midspan of the beam with length  $\frac{1}{4}$  the maximum aggregate size (maximum aggregate size =  $\frac{3}{8}$  inches). Domain integrals were used to determine mode I and mode II stress intensity factors (Li et al., 1985; Moran and Shih, 1987). Plane strain conditions were assumed; the details are given in Organ (1996).

Simulations were first performed with constant crack velocity  $v = 0.05c_s$  to determine whether the transition point  $\gamma_t$  could be ascertained by the numerical model. Three representative crack paths for these simulations are shown in Fig. 41, and the evolution of the cracks in one simulation is shown in Fig. 42. The crack emanating from the notch tended to *turn away from the load point*, in contrast to the experiments in Fig. 40 in which the notches curved toward the load point. The simulations did not exhibit a crisp transition from crack growth at the notch to crack growth at the midspan. Instead, for a range  $\gamma_{t_1} < \gamma < \gamma_{t_2}$ , both cracks propagate as shown in Fig. 41(b). The transition occurs over a range of  $0.672 < \gamma < 0.734$ . The time histories of the mode I and II stress intensity factors are shown in Fig. 43 for the notch at  $\gamma = 0.672$ .

Next we considered the case where the crack velocity was governed by  $K_{I_{eq}}(v) = K_{I_c}(v)$ . For this case, the crack path *curved toward the load point* which more closely matches the experimental results; compare Fig. 44 to the constant velocity solution in Fig. 41a and the experimental results in Fig. 40.

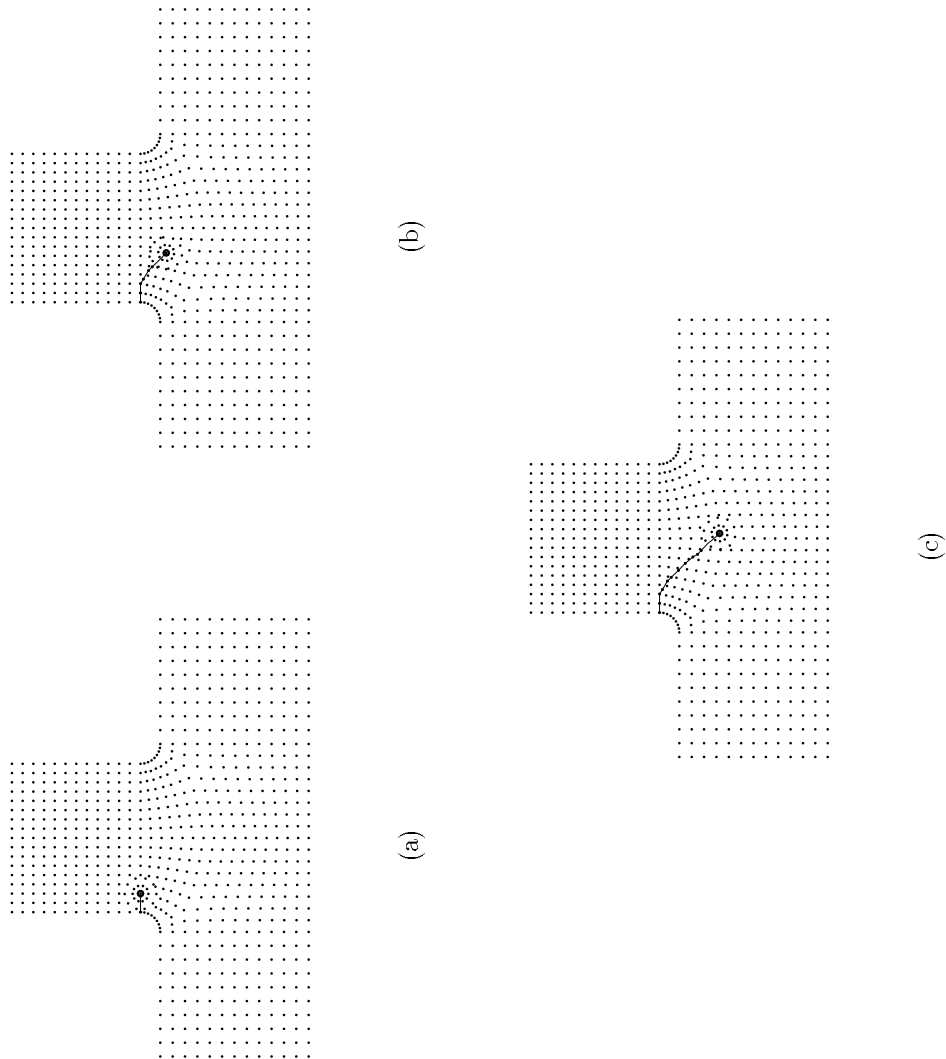


Figure 35: Crack path progression from a fillet for the case of a thin I-beam.

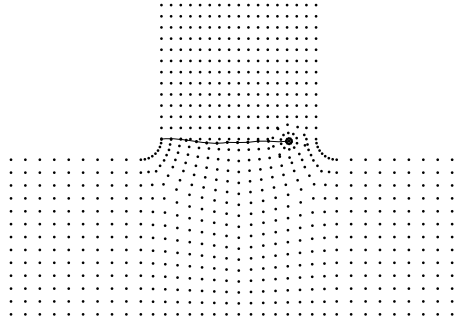


Figure 36: Crack path from a fillet for case of a thick I-beam.

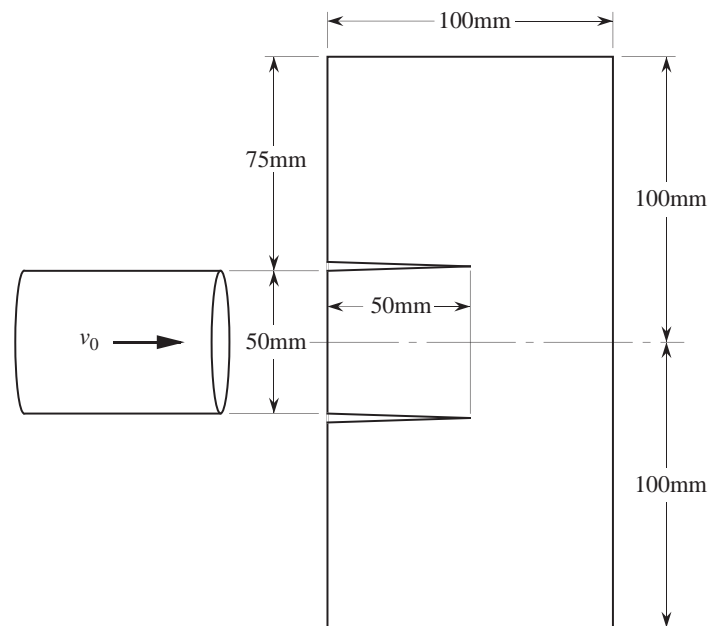


Figure 37: Experimental setup for the experiments by Kalthoff and Winkler (1987).

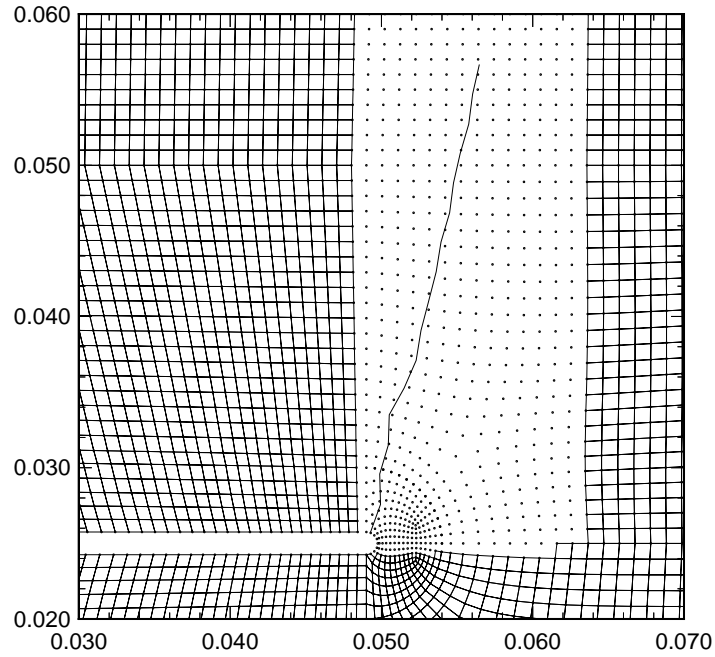


Figure 38: Crack path for the edge-cracked plate by the coupled FE-EFG method.

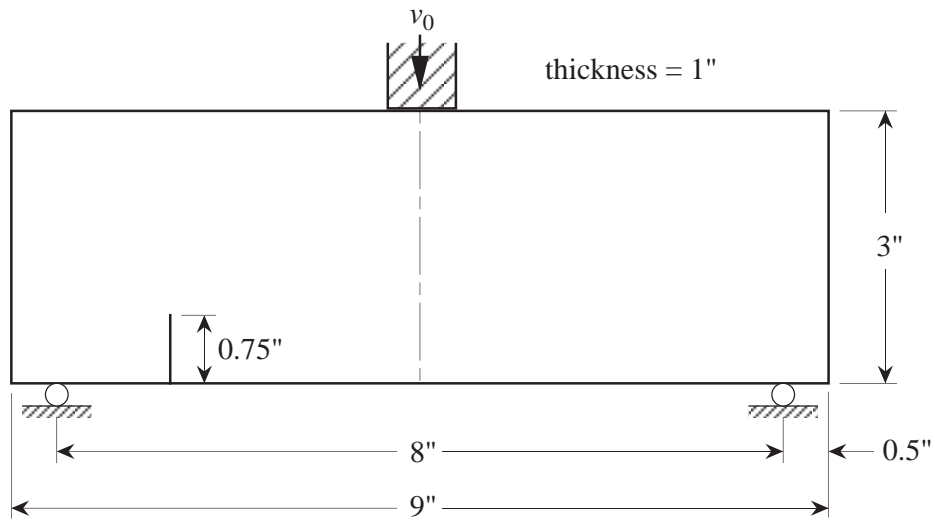


Figure 39: 3-point-bend specimen with offset notch.

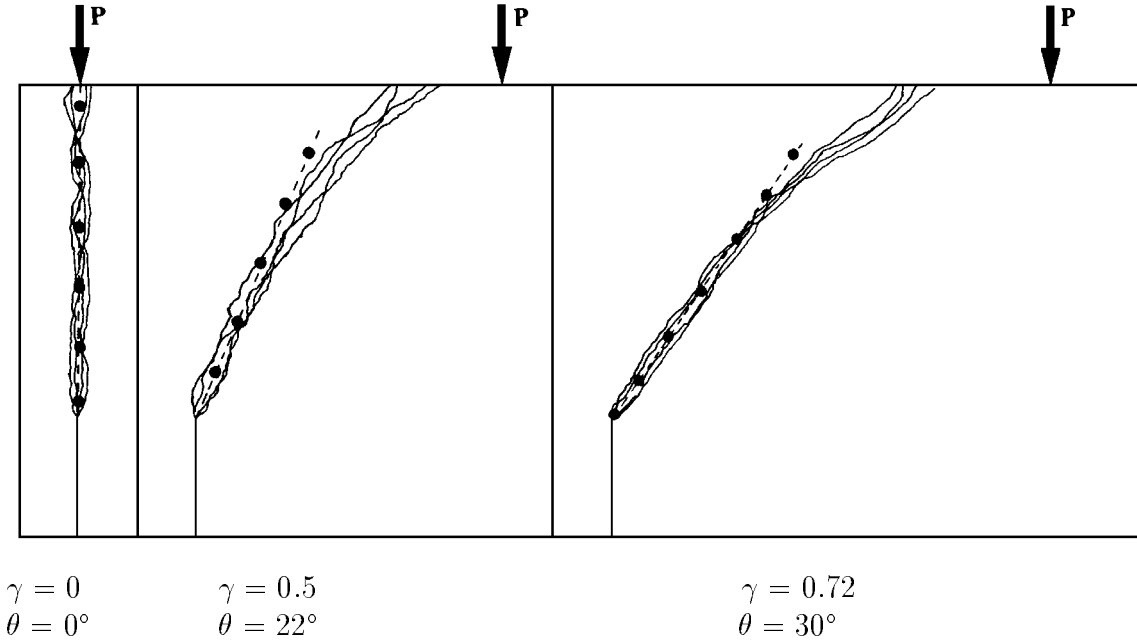


Figure 40: Experimental crack paths reported by John (1988). The dashed lines are the initial directions  $\theta$  predicted by linear elastic fracture mechanics. Angles  $\theta$  are measured from the vertical.

## 7.5 Taylor Bar 3D Computation

The EFG method was applied to the Taylor bar, a classical benchmark for nonlinear computations; see, e.g., Hallquist (1980) and Liu et al. (1988). The present model formulates the problem as a symmetric one: the bar does not impact a wall, but another bar moving with the same velocity in the opposite direction. The material is copper, and the computational model is classical  $J_2$  flow with linear isotropic hardening:  $E = 117$  GPa,  $\nu = 0.35$ ,  $\rho = 8930$  kg/m<sup>3</sup>,  $h = 100$  MPa,  $\sigma_{y0} = 400$  MPa. The radius of the cylinder is 3.2 mm, and its length is 32.4 mm. The uniform initial velocity is 227 m/s. The response is computed for 80  $\mu$ sec, since by this time the kinetic energy is almost entirely dissipated.

Fig. 45 shows the deformed mesh at 80  $\mu$ sec. The numerical model consists of a background cell structure with one EFG node at the center of each cell; a surface representation is not included yet. The full model consists of 800 nodes (2400 degrees of freedom), and 480 hexahedral integration cells. One point quadrature was used with the exception of the 5 layers of cells nearest to the impact plane, where  $2 \times 2 \times 2$  quadrature was applied. Explicit time integration was used with  $\Delta t = 0.1 \mu$ sec.

The results at  $t = 80 \mu$ sec as compared to the 3D solution of Hallquist (1980) computed by DYNA3D are: radius at the plane of impact: 6.96 mm (DYNA3D: 7.03 mm), final length: 21.63 mm (DYNA3D: 21.47 mm). Fig. 45 shows a cut through

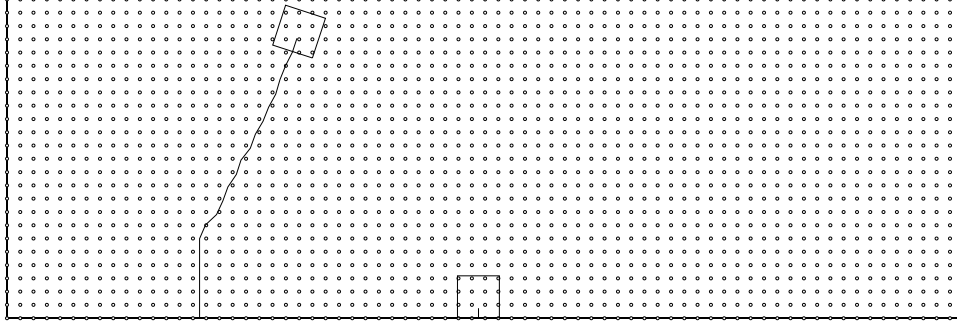
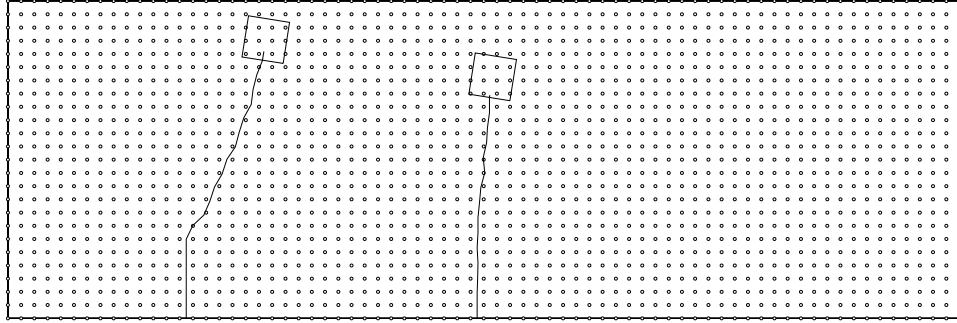
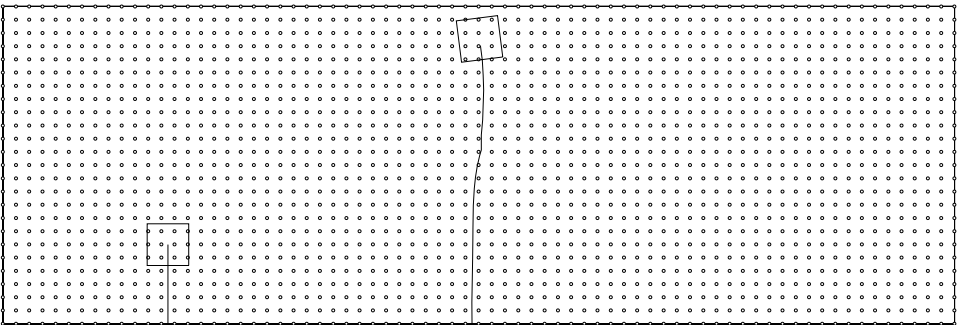
(a)  $\gamma = 0.672$ (b)  $\gamma = 0.703$ (c)  $\gamma = 0.734$ 

Figure 41: Final crack configurations and J-integral domains. Solutions were generated using constant crack velocity:  $v_c = 0.5c_s$ .



Figure 42: Evolution of a notch at  $\gamma = 0.703$  and a midspan crack propagating at constant crack velocity,  $v_c = 0.05c_s$ .

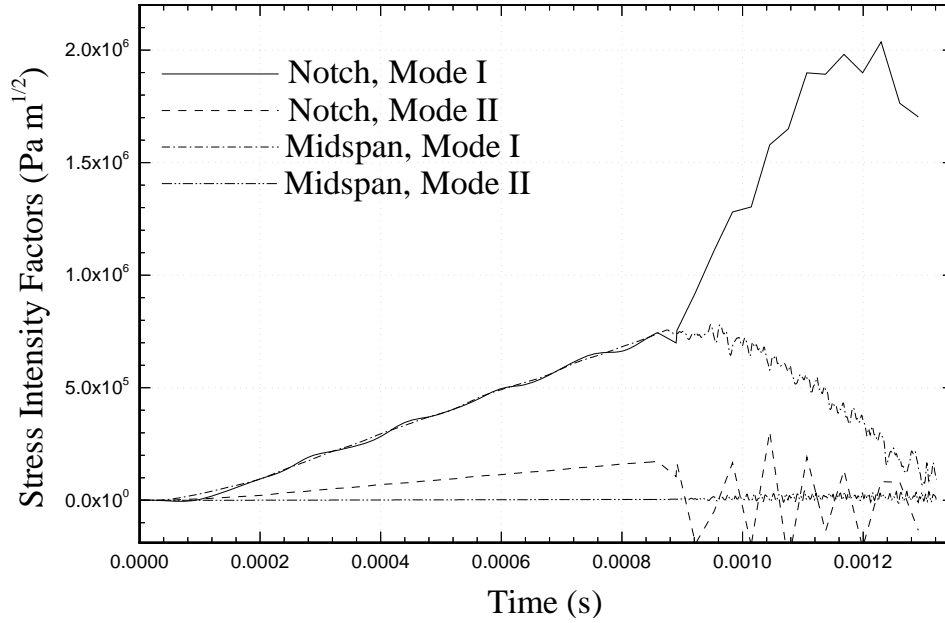


Figure 43: Stress intensity factors at the midspan crack and offset notch at  $\gamma = 0.672$  for constant crack velocity  $v_c = 0.05c_s$ .

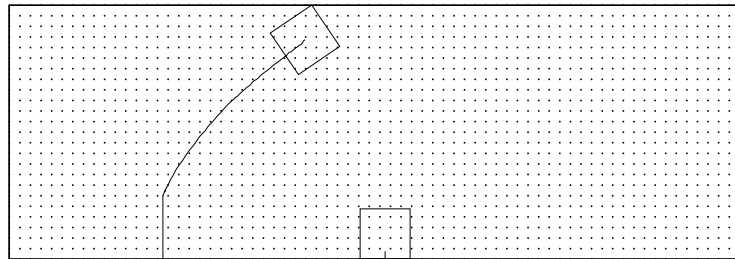


Figure 44: Crack path and J-integral domains for a notch at  $\gamma = 0.672$ . Solution generated with a variable crack velocity.



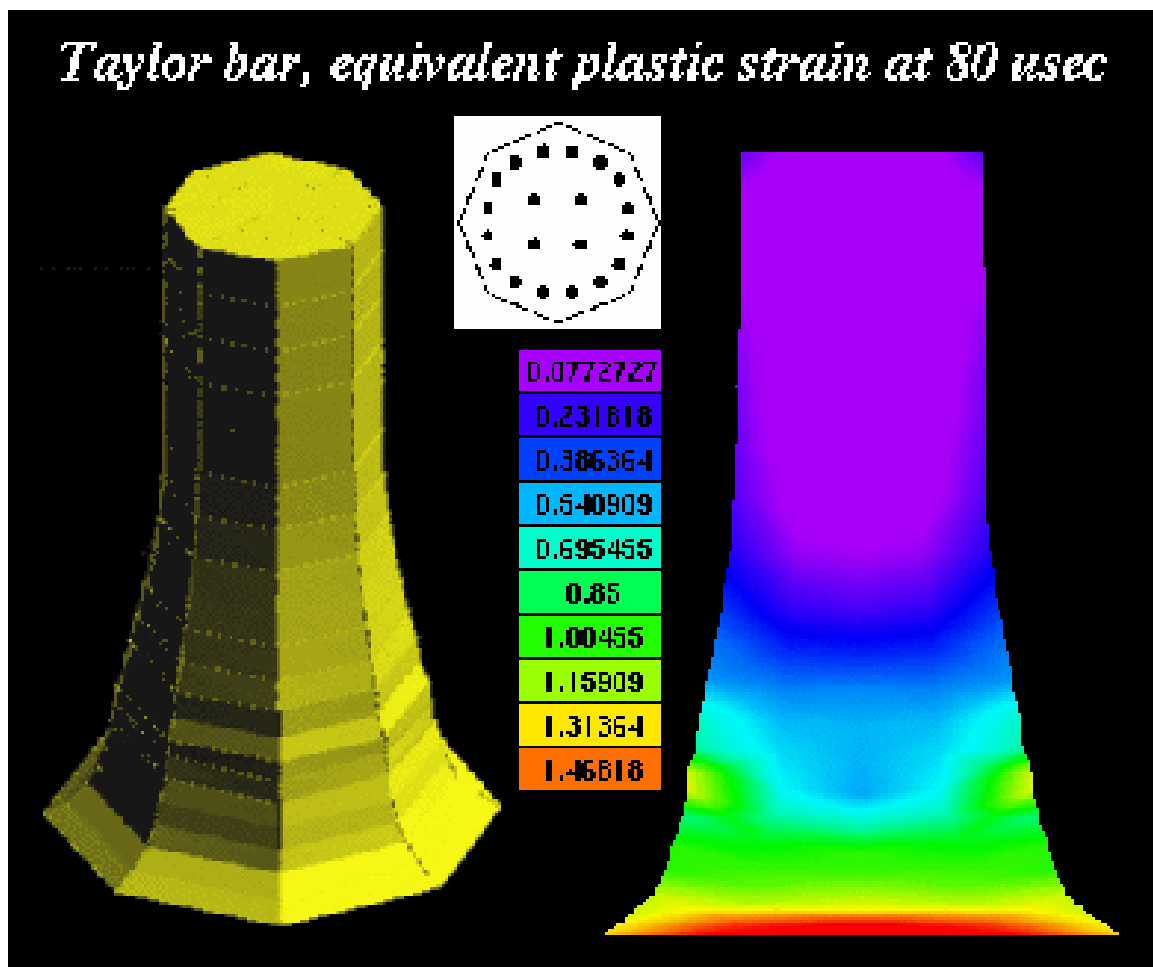


Figure 45: Deformed mesh and equivalent plastic strain at  $80\mu\text{sec}$  for a Taylor bar.

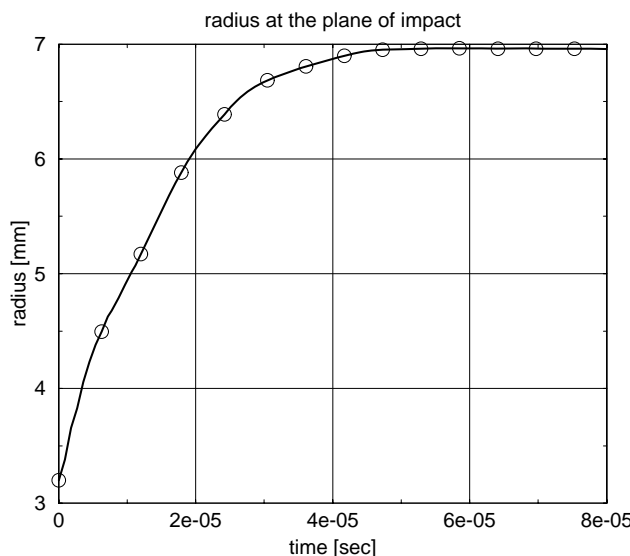


Figure 46: Evolution of the radius at the plane of impact

the deformed mesh at  $t = 80\mu\text{sec}$  with the contours of the equivalent plastic strain, and Fig. 46 shows the evolution of the radius at the impact plane.

## 8 Conclusions

We have presented an overview of meshless methods, focusing on three themes: kernel approximations, moving least squares, and partitions of unity. Each theme provides a different viewpoint for constructing meshless approximations. The approximations constructed by kernel methods and moving least squares are identical once the requirement of consistency is imposed. Those methods can also be viewed as partitions of unity, and partitions of unity provide a more direct means for achieving  $p$ -adaptivity.

We have stressed the topic of the incorporation of discontinuities and the treatment of multiply connected bodies. In this, we were motivated by the requirements of practical problems, where their effective treatment is essential. Furthermore, it is our opinion that the treatment of evolving discontinuities, such as cracks, simplified models of shear band, phase interfaces, and shocks, is the field in which meshless methods have the greatest promise.

Implementation issues have also been discussed at length, for it is in this area that some of the major difficulties remain. Currently, the computational costs of explicit EFG exceeds a low-order finite elements by a factor of 4 to 10; in three-dimensional static problems the disadvantage is even more pronounced. However, the three dimensional comparisons given here indicate that meshless methods can attain

nearly the same accuracy for the same computational cost. Effective implementations of meshless methods are key to their success.

As can be seen from this review, the field is in a state of rapid evolution. Although, meshless methods were discovered almost 20 years ago, it is only recently that they have captured the interests of a broader community of researchers who can bring divergent skills and backgrounds to bear on the task of improving these methods. There are many aspects of meshless methods which could benefit from improvements. For example, the techniques for treating discontinuities, to the best of our knowledge, have only been examined so far by this group and Oden and co-workers. Our approach has been driven by our visibility and light paradigms, but there are undoubtedly other paradigms that are simpler and more effective. Similarly, the relationship to wavelets offers a multitude of possibilities.

Wavelets and current meshless methods are manifestations of the same basic trend toward methods with localized approximations. The counterparts of meshless methods and wavelets in classical analysis are, respectively, global collocation methods and Fourier series, which have serious disadvantages in computer software. The advantage of localized methods is their compatibility with computers and scalability. Finite elements are also a reflection of this trend toward localization in computer methods. However, the highly structured nature of finite element approximations imposes severe penalties in solutions of certain problems, and it is the decrease in structure that makes meshless methods appealing.

Meshless methods still require considerable improvement before they equal the prominence of finite elements and finite differences in computer science and engineering. The greatest challenges appear to be in developing the speed and robustness in meshless methods which characterize low-order finite elements. The quality of the approximations are exemplary, only the cost is too high. Breakthroughs in these directions will have considerable impact.

## Acknowledgments

The support of the Office of Naval Research, the Air Force Office of Scientific Research and Army Research Office is gratefully acknowledged. The support of DOE's CSGF program for Y. Krongauz is also gratefully acknowledged.

## References

- Attaway, S. W., M. W. Heinstein, and J. W. Swegle (1994). Coupling of smooth particle hydrodynamics with the finite element method. *Nuclear Engineering and Design* 150, 199–205.
- Babuška, I. and J. M. Melenk (1995). The partition of unity finite element method. Technical Report BN-1185, Institute for Physical Science and Technology, Uni-

- versity of Maryland.
- Belytschko, T., L. Gu, and Y. Y. Lu (1994). Fracture and crack growth by element-free Galerkin methods. *Modelling and Simulation in Material Science and Engineering* 2, 519–534.
- Belytschko, T., Y. Krongauz, M. Fleming, D. Organ, and W. K. Liu (to appear). Smoothing and accelerated computations in the element-free Galerkin method. *Journal of Computational and Applied Mathematics*.
- Belytschko, T., Y. Y. Lu, and L. Gu (1994). Element-free Galerkin methods. *International Journal for Numerical Methods in Engineering* 37, 229–256.
- Belytschko, T., D. Organ, and Y. Krongauz (1995). A coupled finite element–element-free Galerkin method. *Computational Mechanics* 17, 186–195.
- Belytschko, T., H. Stolarski, W. K. Liu, N. Carpenter, and J. S.-J. Ong (1985). Stress projection for membrane and shear locking in shell finite elements. *Computer Methods in Applied Mechanics and Engineering* 51, 221–258.
- Belytschko, T. and M. Tabbara (1996). Dynamic fracture using element-free Galerkin methods. *International Journal for Numerical Methods in Engineering* 39, 923–938.
- Chu, Y. A. and B. Moran (1995). A computational model for nucleation of solid–solid phase transformations. *Modelling Simul. Mater. Sci. Eng.* 3, 455–471.
- Ciarlet, P. G. (1991). Basic error estimates for elliptic problems. In C. P. G. and J. L. Lions (Eds.), *Handbook of numerical analysis, Vol. II, Finite element methods, Part 1*, Amsterdam. Elsevier, North-Holland.
- Cleveland, W. S. (1993). *Visualizing Data*. Murray Hill, N.J.: AT&T Bell Laboratories, Murray Hill, N.J.
- Cordes, L. W. and B. Moran (submitted). Treatment of material discontinuity in the element-free Galerkin method. *Computer Methods in Applied Mechanics and Engineering*.
- Duarte, C. A. (1996). Personal communication.
- Duarte, C. A. and J. T. Oden (1996).  $H$ - $p$  clouds—an  $h$ - $p$  meshless method. *Numerical Methods for Partial Differential Equations*, 1–34.
- Dyka, C. T. (1994). Addressing tension instability in SPH methods. Technical Report NRL/MR/6384, NRL.
- Fleming, M., Y. A. Chu, B. Moran, and T. Belytschko (1997). Enriched element-free Galerkin methods for crack tip fields. *International Journal for Numerical Methods in Engineering* 40.
- Gosz, J. (1996). Personal communication.

- Hallquist, J. O. (1980). *DYNA2D and DYNA3D user's manuals*. Livermore, CA: Lawrence Livermore National Laboratories.
- Hegen, D. (1994). Numerical techniques for the simulation of crack growth. Technical report, Eindhoven University of Technology. Final report of the postgraduate programme Mathematics for Industry.
- Hein, P. (1993). Diffuse element method applied to Kirchhoff plates. Technical report, Dept. Civil Engrg, Northwestern University, Evanston, IL.
- John, R. (1988). *Mixed Mode Fracture of Concrete Subjected to Impact Loading*. Ph. D. thesis, Northwestern University.
- John, R. and S. P. Shah (1990). Mixed mode fracture of concrete subjected to impact loading. *ASCE Journal of Structural Engineering* 116, 585–602.
- Johnson, G. R. (1994). Linking Lagrangian particle methods to standard finite element methods for high velocity impact computations. *Nuclear Engineering and Design* 150, 265–274.
- Johnson, G. R. and S. R. Beissel (1996). Normalized smoothing functions for SPH impact computations. *International Journal for Numerical Methods in Engineering*.
- Kalthoff, J. F. and S. Winkler (1987). Failure mode transition at high rates of shear loading. In C. Y. Chiem, H. D. Kunze, and L. W. Meyer (Eds.), *International Conference on Impact Loading and Dynamic Behavior of Materials*, Volume 1, pp. 185–195.
- Krongauz, Y. and T. Belytschko (submitted,a). Consistent pseudo-derivatives in meshless methods. *Computer Methods in Applied Mechanics and Engineering*.
- Krongauz, Y. and T. Belytschko (submitted,b). EFG approximation with discontinuous derivatives. *International Journal for Numerical Methods in Engineering*.
- Krongauz, Y. and T. Belytschko (to appear). Enforcement of essential boundary conditions in meshless approximations using finite elements. *Computer Methods in Applied Mechanics and Engineering*.
- Krysl, P. and T. Belytschko (1996a). Analysis of thin plates by the element-free Galerkin method. *Computational Mechanics* 17, 26–35.
- Krysl, P. and T. Belytschko (1996b). Analysis of thin shells by the Element-Free Galerkin method. *Int. J. Solids & Structures* 33, 3057–3080.
- Krysl, P. and T. Belytschko (to appear). Element-free Galerkin method: Convergence of the continuous and discontinuous shape functions. *Computer Methods in Applied Mechanics and Engineering*.
- Lancaster, P. and K. Salkauskas (1981). Surfaces generated by moving least squares methods. *Mathematics of Computation* 37, 141–158.

- Li, F. Z., C. F. Shih, and A. Needleman (1985). A comparison of methods for calculating energy release rates. *Engineering Fracture Mechanics* 21(2), 405–421.
- Liszka, T. and J. Orkisz (1980). The finite difference method at arbitrary irregular grids and its application in applied mechanics. *Computers and Structures* 11, 83–95.
- Liu, W. K., H. Chang, J. S. Chen, and T. Belytschko (1988). Arbitrary Lagrangian-Eulerian Petrov-Galerkin finite elements for non-linear continua. *Computer Methods in Applied Mechanics and Engineering* 68, 259–310.
- Liu, W. K. and Y. Chen (1995). Wavelet and multiple scale reproducing kernel methods. *International Journal for Numerical Methods in Fluids* 21, 901–931.
- Liu, W. K., Y. Chen, C. T. Chang, and T. Belytschko (1996). Advances in multiple scale kernel particle methods. *Computational Mechanics, An International Journal*.
- Liu, W. K., Y. Chen, S. Jun, J. S. Chen, T. Belytschko, C. Pan, R. A. Uras, and C. T. Chang (1996). Overview and applications of the reproducing kernel particle methods. *Archives of Computational Methods in Engineering: State of the art reviews* 3, 3–80.
- Liu, W. K., Y. Chen, and R. A. Uras (1995). Enrichment of the finite element method with the reproducing kernel particle method. In J. J. F. Cory and J. L. Gordon (Eds.), *Current Topics in Computational Mechanics*, Volume 305, pp. 253–258. ASME-PVP.
- Liu, W. K., S. Jun, S. Li, J. Adey, and T. Belytschko (1995). Reproducing kernel particle methods for structural dynamics. *International Journal for Numerical Methods in Engineering* 38, 1655–1679.
- Liu, W. K., S. Jun, and Y. F. Zhang (1995). Reproducing kernel particle methods. *International Journal for Numerical Methods in Engineering* 20, 1081–1106.
- Liu, W. K., S. Li, and T. Belytschko (1996). Reproducing least square kernel Galerkin method. (i) Methodology and convergence. *Computer Methods in Applied Mechanics and Engineering*. in preparation.
- Lu, Y. Y., T. Belytschko, and L. Gu (1994). A new implementation of the element free Galerkin method. *Computer Methods in Applied Mechanics and Engineering* 113, 397–414.
- Lu, Y. Y., L. Gu, and T. Belytschko (1996). Internal report.
- Lucy, L. B. (1977). A numerical approach to the testing of the fission hypothesis. *The Astronomical Journal* 82(12), 1013–1024.
- Monaghan, J. J. (1982). Why particle methods work. *SIAM Journal of Scientific and Statistical Computing* 3(4), 422–.

- Monaghan, J. J. (1988). An introduction to SPH. *Computer Physics Communications* 48, 89–96.
- Monaghan, J. J. (1992). Smooth particle hydrodynamics. *Annual Review of Astronomy and Astrophysics* 30, 543–574.
- Moran, B. and C. F. Shih (1987). Crack tip and associated domain integrals from momentum and energy balance. *Engineering Fracture Mechanics* 27(6), 615–641.
- Nayroles, B., G. Touzot, and P. Villon (1992). Generalizing the finite element method: diffuse approximation and diffuse elements. *Computational Mechanics* 10, 307–318.
- Oñate, E., S. Idelsohn, O. C. Zienkiewicz, R. L. Taylor, and C. Sacco (submitted). A stabilized finite point method for analysis of fluid mechanics problems.
- Organ, D. (1996). *Numerical Solutions to Dynamic Fracture Problems using the Element-Free Galerkin Method*. Ph. D. thesis, Northwestern University.
- Organ, D., M. Fleming, T. Terry, and T. Belytschko (1996). Continuous meshless approximations for nonconvex bodies by diffraction and transparency. *Computational Mechanics* 18, 1–11.
- Perrone, N. and R. Kao (1975). A general finite difference method for arbitrary meshes. *Computers and Structures* 5, 45–58.
- Shepard, D. (1968). A two-dimensional interpolation function for irregularly spaced points. In *ACM National Conference*, pp. 517–524.
- Strang, G. and G. Fix (1973). *An Analysis of the Finite Element Method*. Englewood Cliffs, N.J.: Prentice-Hall.
- Stummel, F. (1979). The generalized patch test. *SIAM J. Numer. Analysis* 3, 449–471.
- Sumi, Y. (1985). Computational crack path prediction. *Theoretical and applied fracture mechanics* 4, 149–156.
- Sumi, Y., S. Nemat-Nasser, and L. M. Keer (1985). On crack path stability in a finite body. *Engineering Fracture Mechanics* 22, 759–771.
- Sumi, Y., C. Yang, and Z. N. Wang (submitted). Morphological aspects of fatigue crack propagation part ii—effects of stress biaxiality and welding residual stress.
- Swegle, J. W., D. L. Hicks, and S. W. Attaway (1995). Smoothed particle hydrodynamics stability analysis. *Journal of Computational Physics* 116, 123–134.
- Timoshenko, S. P. and J. N. Goodier (1970). *Theory of Elasticity* (Third ed.). New York: McGraw Hill.
- Yagawa, G. (1995). Some remarks on free mesh method: A kind of meshless finite element method. In *International Conference on Computational Engineering Science*, Hawaii, USA.